# The soft X-ray properties of quasars in the Sloan Digital Sky Survey

Shiyin Shen[1,2,3], Simon D.M. White[2], H.J. Mo[4], Wolfgang Voges[3],

Guinevere Kauffmann[2], Christy Tremonti[5], Scott F. Anderson[6] ⋆

[1] *Shanghai Astronomical Observatory, Chinese Academy of Sciences, Shanghai 200030, China*
[2] *Max-Planck-Institut für Astrophysik, Karl Schwarzschild Str. 1, Postfach 1317, 85741 Garching, Germany*
[3] *Max-Planck-Institut für extraterrestrische Physik, Postfach 1312, 85741 Garching, Germany*
[4] *Department of Astronomy, University of Massachusetts, Amherst MA 01003-9905, USA*
[5] *Steward Observatory, 933 N Cherry Ave, Tucson, AZ 85721, USA*
[6] *Department of Astronomy, University of Washington, Box 351580, Seattle, WA 98195, USA*

5 February 2008

**ABSTRACT**
We use the ROSAT All Sky Survey (RASS) to study the soft X-ray properties of a homogeneous sample of 46,420 quasars selected from the third data release of the Sloan Digital Sky Survey (SDSS). Optical luminosities, both at rest-frame 2500Å ($L_{2500}$) and in [OIII] ($L_{\text{[OIII]}}$) span more than three orders of magnitude, while redshifts range over $0.1 < z < 5.4$. We detect 3366 quasars directly in the observed 0.1–2.4 keV band. Sub-samples of radio-loud and radio-quiet objects (RLQs and RQQs) are obtained by cross-matching with the FIRST catalogue. We study the distribution of X-ray luminosity as a function of optical luminosity, redshift and radio power using both individual detections and stacks of complete sets of similar quasars. At every optical luminosity and redshift $\log L_{2\text{keV}}$ is, to a good approximation, normally distributed with dispersion $\sim 0.40$, at least brightwards of the median X-ray luminosity. This median X-ray luminosity of quasars is a power law of optical luminosity with index $\sim 0.53$ for $L_{2500}$ and $\sim 0.30$ for $L_{\text{[OIII]}}$. RLQs are systematically brighter than RQQs by about a factor of 2 at given optical luminosity. The zero-points of these relations increase systematically with redshift, possibly in different ways for RLQs and RQQs. Evolution is particularly strong at low redshift and if the optical luminosity is characterised by $L_{\text{[OIII]}}$. At low redshift and at given $L_{\text{[OIII]}}$ the soft X-ray emission from type II AGN is more than 100 times weaker than that from type I AGN.

**Key words:** galaxies: active - galaxies: evolution - galaxies: nuclei - quasars general - X-rays: galaxies - X-rays: general

## 1 INTRODUCTION

Quasars show strong emission at both ultraviolet (UV) and X-ray wavelengths. Indeed, many quasar catalogues have been constructed on the basis of their UV and X-ray properties (e.g. Schneider et al. 2003, 2005; Wolf et al. 2004). The relation between the UV and X-ray continuum emission is usually characterized by a spectral index,

$$\alpha_{OX} \equiv -\frac{\log\left(L_{2\text{keV}}/L_{2500}\right)}{\log\left(\nu_{2\text{keV}}/\nu_{2500}\right)} = -0.384\log\left(L_{2\text{keV}}/L_{2500}\right), \quad (1)$$

where $L_{2\text{keV}}$ and $L_{2500}$ are luminosities per unit frequency at wavelengths of 2 keV and 2500Å, respectively.

⋆ E-mail: ssy@shao.ac.cn

Previous investigations have indicated that the value of $\alpha_{OX}$ changes systematically with optical luminosity $L_O$ (e.g. Zamorani et al. 1981; Avni & Tananbaum 1982, 1986; Bechtold et al. 1994; Pickering, Impey & Foltz 1994; Avni, Worrall & Morgan 1995; Green et al. 1995; Vignali, Brandt & Schneider 2003a; Anderson et al. 2004 and references therein). Most of these studies also concluded that $\alpha_{OX}$ depends only weakly on redshift, but separation of the redshift and luminosity dependences is difficult because of the strong correlation between the two quantities in flux-limited samples (e.g. Anderson & Margon 1987; Bechtold et al. 2003). A dependence of $\alpha_{OX}$ on $L_O$ implies that the relation between $L_X$ and $L_O$ is nonlinear, the trend in the observational data being represented by a power law,

$$L_X \propto L_O^e, \quad (2)$$

with $e < 1$. However, this trend can be affected by a variety of observational factors, for example, sample definition, sample completeness, observational errors, and the adopted fitting method. Consequently, the exact form of the mean $L_X$-$L_O$ relation is still controversial (Franceschini et al. 1994; Yuan et al. 1998; Vignali et al. 2003b). In particular, as pointed out by La Franca et al. (1995) and Yuan, Siebert & Brinkmann (1997), for some earlier datasets it was conceivable that large photometric errors in the optical luminosities had biased an intrinsically linear relation into an apparently nonlinear one.

In order to establish the $L_O$-$L_X$ relation robustly, a large and homogeneous quasar sample with accurate optical and X-ray measurements is required. The quasar catalogue selected from the SDSS (York et al. 2000) third data release (DR3) includes more than 46,000 quasars (Schneider et al. 2005) and is currently by far the largest available (as of July 2005). The SDSS quasar selection algorithm is quite efficient, and the completeness at $z < 3$ is at least 90 percent (Richard et al. 2002; Vanden Berk et al. 2005). Deep surveys which can be used to select X-ray AGN to faint limits cover small areas of the sky (e.g. Wolf et al. 2004) and so overlap at most a small fraction of the SDSS data (e.g. Risaliti & Elvis 2005). On the other hand, the ROSAT All-Sky Survey (RASS) is quite shallow, with an average exposure time of about $\sim$ 400s, and does not detect most SDSS quasars individually. It is possible, however, to detect these objects statistically by stacking their X-ray images. Such stacking is widely used in X-ray astronomy for objects which are individually below the detection limit (e.g. Wu & Anderson 1992; Schartel et al. 1996; Nandra et al. 2002; Georgakakis et al. 2003). Since the number of SDSS quasars is large, the detection limits can be greatly improved by stacking many objects with similar optical properties.

Different classes of quasars are observed to have different X-ray properties. For example, radio-loud objects are systematically brighter in X-rays than radio-quiet ones (e.g. Ku, Helfand & Lucy 1980; Zamorani et al. 1981; Bassett et al. 2004). Type II quasars are usually much weaker in the soft X-ray band than type I objects, presumably due to stronger absorption (e.g. Zakamska et al. 2004; Vignali, Alexander & Comastri 2004). BL Lacertae (BL Lac) objects show strong and rapid variability in all bands. In combination, the RASS and the large quasar catalogue provided by SDSS enable a comparative study of quasars in these different categories.

In this paper, we use the RASS to study the soft X-ray properties of the SDSS DR3 quasars. Optical properties for the sample are derived from the SDSS photometry and spectroscopy. We will make particular use of the continuum luminosity at 2500Å rest wavelength $L_{2500}$ and the [OIII]$\lambda5007$ line luminosity $L_{[OIII]}$, both of which can be determined accurately for large samples of quasars. Our analysis considers X-ray fluxes both for individually detected quasars, and for stacks of quasars of similar redshift and optical luminosity. We develop statistical methods specifically designed to study the joint distribution of soft X-ray and optical properties in the SDSS-RASS samples. In addition, we use the FIRST survey (Becker, White & Helfand 1995) to split the SDSS quasars into radio-loud and radio-quiet classes, and we study the X-ray properties of these two sub-samples separately. The SDSS quasar catalogue does not include type

II and BL Lac objects (Schneider et al. 2005), but a sample of nearby type II AGN has been constructed from the SDSS galaxy catalogues by Kauffmann et al. (2003). We will use this sample to measure the average soft X-ray luminosities of such objects.

Our paper is organized as follows. In Section 2 we introduce the SDSS DR3 quasar sample and explain how we define their optical and radio properties. Section 3 describes our RASS detection technique, both for individual objects and for stacks. In Section 4, we use a variety of techniques to study the joint $L_X - L_O$ distribution. We derive mean relations from complete sets of X-ray detections of stacks spanning the full redshift and optical luminosity range of the sample. We use individual detections to study the high luminosity tail of the distribution of X-ray luminosity at given optical luminosity. We use complete sets of detections for stacks of objects which are *not* individually detected to study the lower luminosity part of this distribution. All approaches give consistent results. We also split the quasar sample in various ways to examine the dependence of the relation on redshift, on radio emission strength and on the presence or absence of broad optical emission lines. We discuss our results and draw our conclusions in Section 5.

## 2    SAMPLE

### 2.1    Optical properties

The SDSS DR3 quasar catalogue consists of 46,420 objects with luminosities brighter than $M_i = -22$, with at least one emission line with FWHM (Full Width at Half Maximum) larger than 1000km s$^{-1}$ and with highly reliable redshifts. (Throughout we will assume the standard $\Lambda-$cosmology with $H_0 = 70$km s$^{-1}$ Mpc$^{-1}$, $\Omega_0 = 0.3$, $\Omega_\Lambda = 0.7$.) A few unambiguous broad absorption line quasars are also included. The sky coverage of the sample is about 4188 deg$^2$ and the redshifts range from 0.08 to 5.41. The five-band $(u, g, r, i, z)$ magnitudes have typical errors of about 0.03 mag. The spectra cover the wavelength range from 3800 to 9200Å, with a resolution of about 1800-2000 (see Schneider et al. 2005 for details).

We use $L_{2500}$, the continuum luminosity at rest wavelength 2500Å, to characterize the near-UV luminosities of quasars. We measure the rest-frame 2500Å monochromatic continuum flux, $f_\lambda(2500\text{Å})$, directly from the SDSS spectra for the quasars with $2500(1 + z)$Å in the SDSS spectroscopic range 3800-9100Å. For quasars outside this redshift range we assume the shape of the spectrum to be the same as that of the composite quasar spectrum presented by Vanden Berk et al. (2001) and we normalize using the rest-frame continuum flux at 3700Å and 1470Å for low$(z < 0.5)$ and high$(2.7 < z < 5.25)$ redshift quasars respectively. For the few quasars at $z > 5.25$, the rest-frame continuum flux at 1360Å is used to normalize the spectra. Following Strateva et al. (2005), we use the Schlegel, Finkbeiner & Davis(1998) extinction maps to estimate Galactic reddening $E(B - V)$ at the position of each quasar and the extinction law of Nandy et al. (1975) to estimate the Galactic extinction $A_\lambda$ at $2500(1+z)$Å or at the relevant normalizing wavelength for each quasar. In addition to a strong UV continuum, most quasars are also characterized by broad emission lines. In
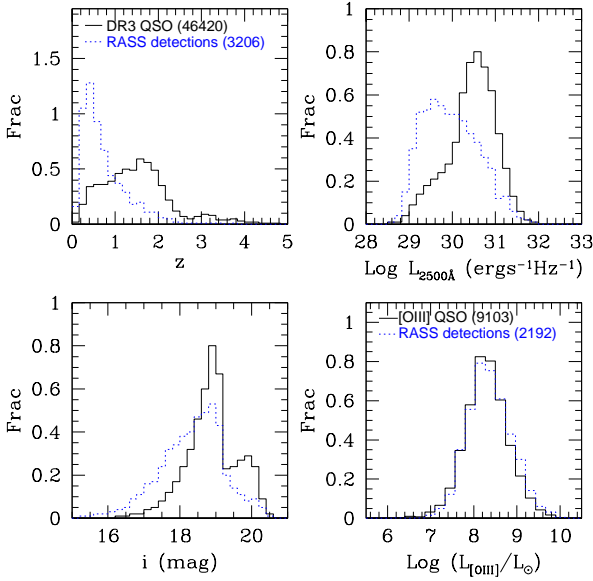
**Figure 1.** The distributions of quasars in the SDSS DR3 catalog with respect to some basic parameters: redshift (upper left), rest-frame 2500Å luminosity (upper right), $i-$band apparent magnitude (lower left), and [OIII] line luminosity (lower right). The solid lines show results for the full sample whereas the dotted lines show the results for quasars with individual RASS detections (see Section 3.1). All the histograms are normalised to unit total area.

**Figure 2.** Our sub-samples of radio-loud and radio-quiet quasars. The top two panels show the $z$ and $R_i$ distributions of DR3 quasars with a FIRST catalogue match. The bottom two panels show histograms of the $L_{2500}$ and $L_{[OIII]}$ distributions for radio-loud (RLQ; red) and radio-quiet (RQQ; blue) quasars. For comparison, the $z$, $L_{2500}$ and $L_{[OIII]}$ distributions for the full sample of DR3 quasars are shown by dotted lines. All the histograms are normalised to unity.

this study, we use the [OIII]$\lambda$5007 line luminosity $L_{[OIII]}$ (again corrected for Galactic extinction) as a measure of the strength of this emission. Due to the SDSS wavelength coverage, [OIII]$\lambda$5007 can be measured only for quasars at $z < 0.8$. There are 9103 such objects.

To illustrate the general properties of the SDSS DR3 quasar sample, we show in Fig. 1 their distributions in redshift $z$, in luminosity $L_{2500}$, and in $i$-band apparent magnitude. The drop at $i \sim 19.1$ roughly corresponds to the completeness limit of the low redshift ($z < 3$) multi-colour selected sample (Richards et al. 2002). The $L_{[OIII]}$ distribution of the low-redshift objects is shown in the lower right panel. These plots also show the distribution for quasars detected individually in the RASS. These objects are clearly biased towards low redshifts, low continuum luminosities and bright apparent magnitudes. Interestingly, there is no apparent bias in the line luminosity distribution.

## 2.2 Radio properties

The X-ray properties of radio-loud quasars (RLQs) and radio-quiet quasars(RQQs) are significantly different. Compared with RQQs, RLQs are characterized by higher X-ray luminosities and flatter X-ray spectra at given optical luminosity (e.g. Worrall et al. 1987; Green et al. 1995; Schartel et al. 1996; Brinkmann et al. 2000; Bassett et al. 2004). However, RLQs are a small minority of the quasar population, only about ten percent of the total (Brinkmann et al. 2000; Ivezic et al. 2002).

In the DR3 quasar catalogue, there are 3757 objects having FIRST matches within the matching radius 2.0 arc-
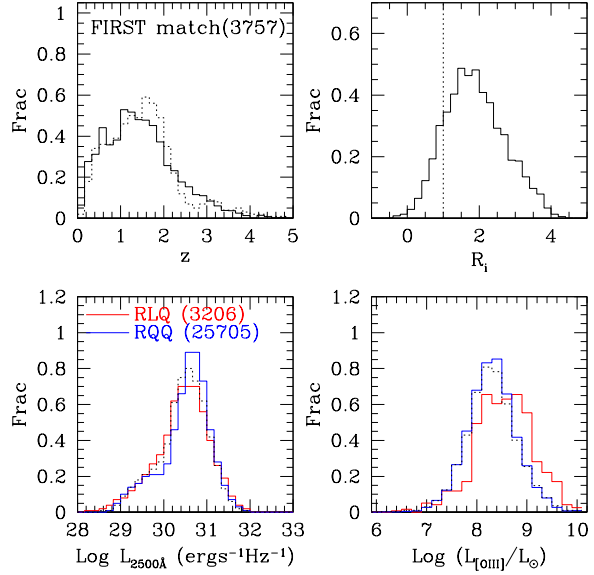
sec. We show the redshift distribution of these objects in the top left panel of Fig. 2. In the sky covered by both the SDSS DR3 and FIRST, there are 37980 quasars without a FIRST match. Unlike the RASS quasars, the $z$ distribution of the FIRST quasars is almost the same as that for the general catalogue (dotted line), which suggests that the optical-to-radio spectral index does not depend strongly on redshift or optical luminosity.

Ivezic et al. (2002) have investigated the radio properties of SDSS objects in detail and suggest a bimodal distribution of radio-to-optical flux ratio, $R_i$, which separates RQQs from RLQs at $R_i \sim 1$ . Here $R_i$ is defined as

$$R_i = \log\left(F_{radio}/F_{optical}\right) = 0.4(m_i - t)$$
$$\text{with} \quad t = -2.5\log\left(\frac{F_{int}}{3631\,\text{Jy}}\right), \tag{3}$$

where $m_i$ is the $i$-band magnitude, $t$ is the AB radio magnitude, and $F_{int}$ is the integrated 20 cm continuum flux density listed in the FIRST catalogue. We show the $R_i$ distribution of the 3757 FIRST quasars in the top right panel of Fig. 2.

We select quasars with $R_i > 1$ as RLQs, giving a sample of 3206 objects. Since the FIRST sensitivity limit of 1mJy corresponds to $t \approx 16.4$ (Ivezic et al. 2002), bright quasars with $i < 19.1$ within the FIRST sky area but with no FIRST catalogue match have $R_i < 1.08$. We select such objects as RQQs, giving a sample of 25705. Apart from the 3206 RLQs and 25705 RQQs, there are a further 17509 objects with indeterminate radio properties. When studying

quasars without specifying their radio properties, we will use the full sample of 46420 objects. We show the $L_{2500}$ and $L_{\text{[OIII]}}$ distributions of RLQs and RQQs as the blue and red histograms in the lower two panels of Fig. 2. As we can see, although RQQs are selected with a bright magnitude limit ($i < 19.1$) their $L_{2500}$ distribution shows no clear difference from that of the RLQs. However, the $L_{\text{[OIII]}}$ distribution of RLQs is biased somewhat high in comparison with that of RQQs. RLQs tend to have slightly higher equivalent widths of [OIII]$\lambda$5007 than RQQs (e.g. Marziani et al. 2003 ). The numbers of quasars in the RLQ, RQQ and full samples are listed together with the relevant magnitude limits and redshift ranges in Table 1.

## 3   THE X-RAY DATA

### 3.1   Individual X-ray detections

The RASS mapped the sky in the soft X-ray band (0.1–2.4 keV) with an effective exposure time varying between 400 and 40,000s, depending on direction. The angular resolution of the survey is 0.5 arcmin and the total exposure time is $\sim 1.0 \times 10^{7}$ s. Two source catalogues were generated based on RASS images: the Bright Source Catalogue (BSC, Voges et al. 1999) and the Faint Source Catalogue (FSC, Voges et al. 2000). The BSC contains $\sim$ 18,800 objects with detection likelihood $L$ [defined after equ. (5) below] of at least 15, while the FSC includes $\sim$105,900 objects with detection likelihood between 7 and 15. In the DR3 quasar catalogue, the position of each quasar was matched to these two catalogues out to a radius of 30 arcsec. The number of matches is 2672. The contamination from chance superpositions is estimated to be about 1–2 percent. However, since the position of each SDSS quasar is known very well, to better than one acrsec according to Pier et al. (2003), we applied the upper-limit maximum likelihood method (the COMP/UPP command in the MIDAS/EXSAS package) directly to the RASS images to calculate a detection likelihood for each SDSS quasar. To be consistent with the RASS source catalogues, we accept all sources with detection likelihood greater than or equal to 7 as individual X-ray detections.

Our detection algorithm is applied to the RASS-II data, which includes 1,378 sky fields, each having a size of $6.4° \times 6.4°$, and with neighboring fields overlapping at least 0.23 degrees (Voges et al. 1999). The data in each field is binned into a $512 \times 512$ pixel image, each pixel having a size of 45 arcsec in the 0.1–2.4 keV band. A local-detection method is first used to search for source candidates in the map within windows of increasing size, starting from $3 \times 3$ pixels. Identified source candidates are then cut out of the image and a smooth background is built by spline fitting. Using the background and exposure map of each field, the upper-limit maximum likelihood detection method takes into account the position of each photon relative to the position of each source candidate within the extraction radius and so accumulates a source detection likelihood $L$. All photons in the 0.1–2.4 keV band are used and the extraction radius is chosen to be 5 times the FWHM (60 arcsec in RASS) of the point spread function (PSF). With this algorithm, 3366 quasars are detected with $L \geq 7$, which is 26% higher than the number of RASS catalogue matches. This number must still include some contamination from random fluctuations in the background.

To estimate the extent of contamination, we build a mock catalogue with the same number of objects and the same sky coverage as the SDSS DR3 quasar sample. The mock objects have random sky positions except that they avoid disks of radius 30 arcsec centered at the position of each DR3 quasar. Applying our algorithm to this mock catalogue, we get 246 random positions with detection likelihood $L \geq 7$, suggesting that a similar number of our quasar "detections" are spurious. To account for this contamination statistically, we randomly select 246 quasars from our 3366 individual detections, requiring not only the same X-ray flux distribution as the random positions with RASS "detections", but also $z$ and $L_{2500}$ values chosen randomly from those of the entire DR3 sample of 46420 quasars. These 246 quasars are then marked as possible contaminants and are excluded from further analysis. The number of RASS individual detections in the sample we finally analyze is therefore 3120. Of course, there is no reason to identify any particular quasar as spurious. Our exclusion of 246 objects is only intended to be statistically correct.

We showed the distributions of the basic properties of the quasars with RASS individual detections as dotted lines in Fig. 1. Compared with the general SDSS population, these objects are biased towards low redshifts and bright apparent magnitudes.

Among the 3206 RLQs, 379 have RASS individual detections, and the estimated number of contaminants is 36. For the 25705 RQQs, the number of detections and estimated number of contaminants are 2164 and 130, respectively. These numbers are also listed in Table 1. The individual detection fraction is significantly higher for RLQs than for RQQs. As we will show, this is because the RLQs have systematically stronger X-ray emission.

We convert the count rates of quasars with individual RASS detections to fluxes in the 0.1–2.4 keV band using PIMMS[†]. Here we assume the photon energy distribution to be a simple power law, $N(E) \propto E^{-\Gamma}$ with $\Gamma = 2$, and we correct for an absorbing column fixed at the Galactic value for each line-of-sight (Dickey & Lockman 1990). Spectral studies of quasars in the 2–10 keV band give a photon index $\Gamma \sim 1.9$ for radio quiet objects and flatter spectra, $\Gamma \sim 1.6$, for radio-loud objects (e.g. Reeves & Turner 2000). In the soft X-ray band, quasar spectra are known to be steeper but with significant scatter (e.g. Yuan et al. 1997; Brinkmann et al. 1997, 2000). Although the values of $\Gamma$ are quite uncertain, the assumption of a flatter ($\Gamma \sim 1.5$) or a steeper ($\Gamma \sim 2.5$) spectrum only changes the derived flux by a few percent. The flux distribution of the 3120 individual RASS detections in our contamination-corrected sample is shown as a solid histogram in Fig. 3. The peak of the flux distribution is at about $4 \times 10^{-13}$erg cm$^{-2}$ s$^{-1}$, which roughly corresponds to the flux completeness limit of RASS. We discuss the X-ray completeness issue in detail in the next section.

---

[†] \protect\vrulewidth0pt\protect\href{http://heasarc.gsfc.nasa.gov/docs/software/tools/pimms_install.html}{http://heasarc.gsfc.nasa.gov/docs/software/tools/pimms_install.html}
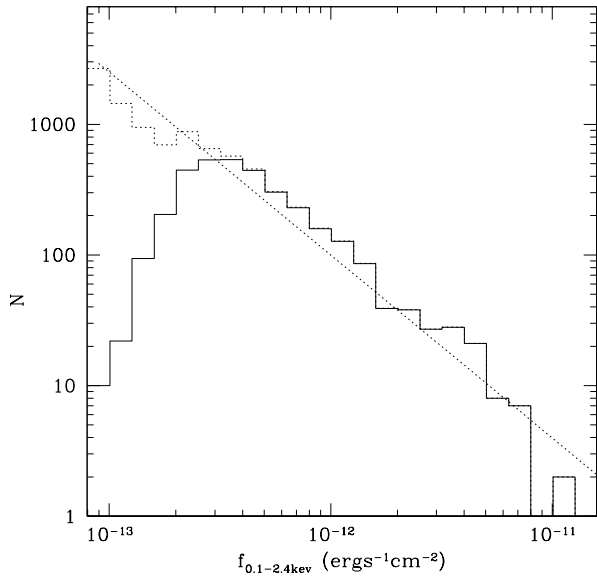
**Figure 3.** Histograms of X-ray flux for our contamination-corrected sample of individually detected DR3 quasars in the 0.1–2.4 keV band. The solid histogram shows the raw data whereas the dotted line indicates the effect of correcting for incompleteness as described in Section 3.2. A dotted straight line with log N–log S slope of −1.4 is shown for comparsion.

## 3.2 Detection completeness

In this section, we consider the completeness of our catalogue of individual RASS detections. Our aim is to figure out the limit above which our sample is complete, and the correction for incompleteness which is needed below this limit.

Whether or not a source of given X-ray flux is detected in the RASS depends on factors such as the effective exposure time, Galactic absorption and background noise. Thus, completeness depends on location in the sky. Since the selection of SDSS quasars is independent of the RASS parameters and the number of these quasars is quite large, their positions can be viewed as a good random realization of the RASS sky inside the DR3 area. The RASS detection completeness $C_{\rm RASS}$ at a given X-ray flux $f$ can thus be defined as [‡]

$$C_{\rm RASS}(f) = \sum_{i=1}^{46420} D_i(f)/46420 \,, \qquad (4)$$

where $D_i$ equals 1 if a source with flux $f$ can be detected by RASS at the position of the $i$th quasar, and $D_i = 0$ otherwise.

More specifically, for an assumed source with flux $f$ at a given position, we calculate the predicted count-rate assuming a photon index $\Gamma = 2$ and the Galactic hydrogen absorption column. The expected number of photons $n_s$ is

[‡] Considering the possible variance of the RASS exposure time and Galactic hydrogen column density over large scales, it is important to note that $C_{\rm RASS}$ as defined here applies only to the sky area of SDSS DR3.
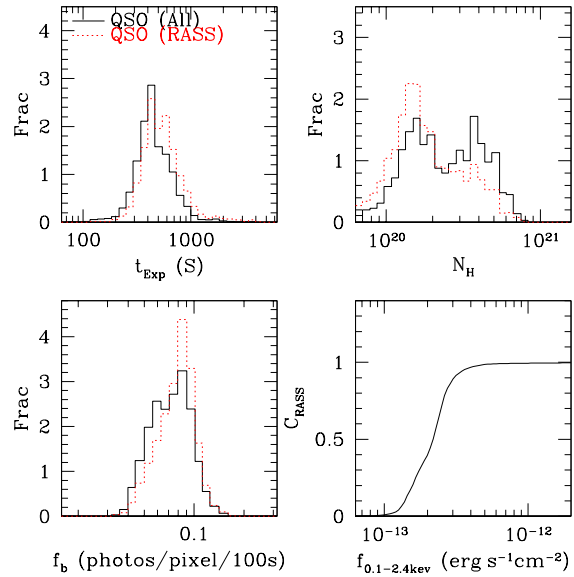


**Figure 4.** The distributions of RASS exposure time, Galactic hydrogen column density and RASS background level at the positions of SDSS quasars (upper left, upper right and lower left respectively). The solid lines show the results for all SDSS DR3 quasars, whereas the dotted lines represent quasars with individual RASS detections. The lower right panel show the RASS detection completeness as a function of X-ray flux. The histograms are normalised to unit enclosed area.

then the product of the effective exposure time at that position and the count-rate. We compare $n_s$ with the local background and define the detection probability $P$ as

$$P = \sum_{n=0}^{n_s+n_b-1} \frac{n_b{}^n}{n!} e^{-n_b} \qquad (5)$$

where $n_b$ is the expected number of background photons inside a circle of 90 arcsec (1.5 times the FWHM, about $3\sigma$ for a Gaussian PSF) surrounding the source position. The simple Poisson counting statistics assumed in equation (5) do not work properly when the number of background photons is very small. For example, a detection with $n_s = 1$ can easily satisfy the condition $L \geq 7$ [$L$ is defined as $L = -\ln(1-P)$] if $n_b$ is very small. We therefore introduce another criterion for a positive source detection,

$$n_s \geq 2.5 + (10 n_b)^{1/2} \qquad (6)$$

which is derived from the maximum likelihood correction for the Eddington Bias (Wang 2004). Objects satisfying both equation (6) and $L \geq 7$ are accepted as individual detections, for which $D_i = 1$. For all other objects, $D_i = 0$.

We show histograms of the Galactic hydrogen column, the RASS effective exposure time and the background level at the position of the 46420 SDSS quasars in Fig. 4. The background level is expressed as the expected number of background photons per pixel for an exposure time of 100 seconds. Distributions for objects with individual detections are also shown for comparison. As one can see, the individually detected objects are biased to longer exposure times and lower Galactic absorption column. The distribution of

the background level is slightly biased to higher values because of the anti-correlation between Galactic hydrogen density and background level. Based on the distribution of the above three quantities, we derive the completeness of our RASS quasar detections as a function of X-ray flux in the 0.1–2.4 keV band from equations (4), (5) and (6). The results are shown in the lower right-hand panel of Fig. 4. Our RASS individual detections are complete to $\sim 98$ percent for $f_{0.1-2.4\mathrm{keV}} > 5.0 \times 10^{-13}\mathrm{erg\,cm^{-2}\,s^{-1}}$. The lower flux limit $f_{\mathrm{lim}}$, at which $C_{\mathrm{RASS}} \sim 0$, is at $\sim 8.0 \times 10^{-14}\mathrm{erg\,cm^{-2}\,s^{-1}}$, consistent with the fact that 3365 of 3366 RASS individual detections have flux greater than $f_{\mathrm{lim}}$. Using $C_{\mathrm{RASS}}$, we can correct for the incompleteness of our RASS individual detections and estimate the true number of quasars at given X-ray flux above $f_{\mathrm{lim}}$. From this, we estimate $\sim 9397$ objects with fluxes greater than $8.0 \times 10^{-14}\mathrm{erg\,cm^{-2}\,s^{-1}}$, as shown in the dotted histogram in Fig. 3. As we can see, the slope of the $\log N$-$\log S$ distribution after correction is close to $-1.4$.

### 3.3 Detection of stacks

As discussed above, only about 7 percent of the SDSS quasars have individual RASS detections because of the limited exposure time. The X-ray properties of the detected quasars are likely to be biased relative to those of the sample as a whole. We have therefore developed a stacking algorithm to study the X-ray properties of the full sample in a way which allows such biases to be understood and corrected.

In general, if the images of $N$ objects are stacked and if we assume these objects all have similar X-ray properties, then the number of photons in the signal increases by a factor of $N$, while the noise from the background fluctuation increases only by a factor of $\sqrt{N}$. Therefore, the signal-to-noise ratio of the stacked image (the stack) is about $\sqrt{N}$ times higher than that of a single image. To proceed, we take the original ($512 \times 512$ pixel) images and exposure maps for the RASS-II fields and cut out small binned images and exposure maps of $65 \times 65$ pixels, centered on the sources to be stacked. Since neighboring RASS fields overlap each other by about 0.23 degrees (18 pixels), a few (less than 1 percent) of the SDSS objects are too close to the image boundaries to make these small images. The small images and the corresponding exposure maps are then added to make the stack. We apply our local detection criterion to the stack using spline fitting to get a smooth background. The photon-event tables of the corresponding binned images are also merged into one table, with the coordinates of all the quasars shifted to be the same. The detector pixel coordinates of all the photon events are kept so as to account for vignetting in the final stack image. With the merged photon table, the stacked exposure map and the background from the stacked image, we apply the same detection method as used for single sources.

For a stack of $N$ sources with Galactic hydrogen density $N_{H,i}$, redshift $z_i$, RASS effective exposure time $t_i$ and X-ray luminosity $L_{2\mathrm{keV},i}$, the number of source photons $N_s$ is

$$N_s = \sum_{i=1}^{N} L_{2\mathrm{keV},i}\ g(N_{H,i}, z_i)t_i\,, \tag{7}$$

where $g(N_{H,i}, z_i)$ is a function which converts the rest-frame X-ray luminosity at 2 keV to observed count-rate. Since the X-ray luminosities of the sources in the stack are supposed to be similar, the weighted average X-ray luminosity of a stack at rest-frame 2 keV is

$$L_{S,2\mathrm{keV}} = \frac{N_s}{\sum_{i=1}^{N} g(N_{H,i}, z_i)t_i}. \tag{8}$$

Only stacks with $L \geq 7$ are accepted as detections. For those with $L < 7$ the photon counts are used to derive upper limits.

## 4 THE SOFT X-RAY PROPERTIES OF SDSS QUASARS

In this section, we investigate how the X-ray properties of SDSS quasars depend on optical luminosity, on redshift and on [OIII] line luminosity, both for our sample as a whole and for our subsamples of radio-loud and radio-quiet quasars. We first present results based on stacks which group all objects with similar optical luminosity and redshift. We then develop a maximum likelihood method which allows individual detections to be used to study the distribution of $L_{2\mathrm{keV}}$ at fixed optical luminosity and redshift. Based on the results, we predict the average $L_{2\mathrm{keV}}$ of quasars *without* individual detections and compare directly with the values measured from stacks of such objects.

### 4.1 Stacks as a function of $L_{2500}$ and $z$

For a first analysis of our data we consider the simple question: what is the mean $L_{2\mathrm{keV}}$ of QSOs of given $L_{2500}$ and how does it depend on redshift? To address this, we stack *all* the sources in each of our chosen luminosity and redshift bins, regardless of whether they are individually detected or not, and we estimate an average X-ray luminosity for the stack. All our quasars are spectroscopically confirmed, so contamination by spurious detections is not an issue for this analysis and we do not exclude the statistically identified "contaminants" from our stacks, which we refer to as "total" stacks in order to distinguish them from the stacks of non-detected sources analysed in Section 4.3 below.

We first divide the sources into seven $\log L_{2500}$ bins from 28.5 to 32.0, with a width of 0.5. The objects in each luminosity bin are then further divided into redshift bins according to the total summed exposure time. Since the X-ray signals from higher redshift quasars are weaker (see Fig. 1), we stack more objects (i.e. require a longer total exposure time) for higher redshift bins. This strategy is illustrated in Fig. 5, where the total exposure time of the stacks of RLQs (triangles) and RQQs (squares) are plotted against their average redshifts. Since the average X-ray luminosity is expected to be weaker for RQQs than for RLQs, we group more objects into one stack in the radio-quiet subsample. We finally get 51 stacks of RLQs and 118 stacks of RQQs.

For the RLQs, we detect 46 stacks with $L > 7$ based on counts in the full 0.1–2.4 keV band but 49 based on counts in the restricted 0.5–2.0 keV band. For RQQs, the numbers of detections in the full and restricted bands are 107 and 117 respectively. The higher detection efficiency in the hard band (0.5–2.0keV) is a result of the weaker background
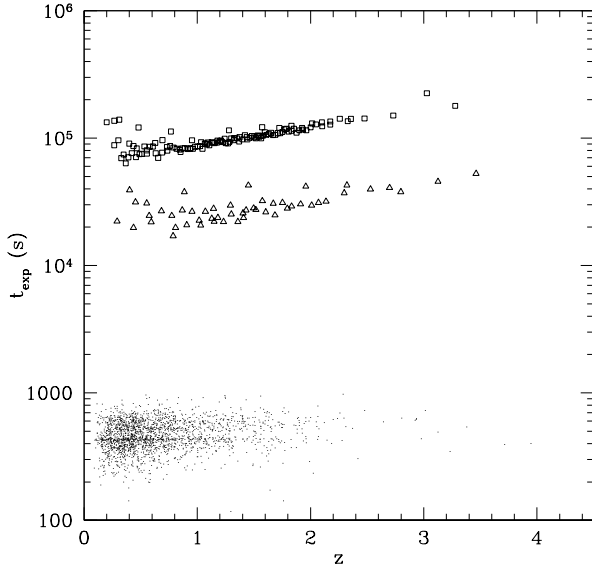
**Figure 5.** Exposure time as a function of redshift for our stacks and for individual sources. The dots show quasars with individual detections whereas the triangles and squares refer to stacks of RLQs and of RQQs respectively.



**Figure 6.** Comparison of the average luminosity of stacks at 2 keV estimated from counts in the full 0.1–2.4 keV band ($L_{2\mathrm{keV}}$) with that estimated from counts in the restricted 0.5–2.0 keV band ($L_{2\mathrm{keV,B}}$). The left two panels show the results for RLQs and the right two for RQQs. The upper panels show a direct comparison between $L_{2\mathrm{keV}}$ and $L_{2\mathrm{keV,B}}$, while the lower panels show the ratio of $L_{2\mathrm{keV}}/L_{2\mathrm{keV,B}}$ as function of the average redshift of the stacks. The solid lines represent the relation $L_{2\mathrm{keV}} = L_{2\mathrm{keV,B}}$.

there (Snowden et al. 1995). To investigate this further we assume that the photon index $\Gamma$ can be taken as constant for all RQQ stacks and for all RLQ stacks, but may differ between the two classes. Using equation (8), we then estimate the average $L_{2\mathrm{keV}}$ of each stack twice, once from the photon counts in 0.1–2.4 keV and once from the counts in 0.5–2.0 keV. We denote the X-ray luminosity estimated from the 0.5–2.0 keV counts by $L_{2\mathrm{keV,B}}$ to distinguish it from $L_{2\mathrm{keV}}$ estimated from the 0.1–2.4 keV counts. By requiring the consistency between $L_{2\mathrm{keV,B}}$ and $L_{2\mathrm{keV}}$, we find that $\Gamma \approx 1.9$ is required for RLQs and $\Gamma \approx 2.1$ for RQQs. This result agrees with the fact that the RLQs show somewhat flatter X-ray spectra than RQQs (e.g. e.g. Worrall et al. 1987; Green et al. 1995; Schartel et al. 1996; Brinkmann et al. 2000; Bassett et al. 2004). With this in mind, in Section 4.2, we will calculate $L_{2\mathrm{keV}}$ for individual detected objects assuming $\Gamma = 1.9$ for RLQs and $\Gamma = 2.1$ for RQQs. We note that in Section 3.1, we used the $\Gamma = 2.0$ to convert the photon counts to fluxes regardless of whether objects are RLQs or RQQs. This slight inconsistency is too small to affect any of our conclusions.

In Fig. 6 we compare $L_{2\mathrm{keV}}$ with $L_{2\mathrm{keV,B}}$ for stacks detected in both bands. The upper panels demonstrate that the two estimates agree to well within their errors both for RLQs and for RQQs. In the lower panels, we plot the ratio $L_{2\mathrm{keV}}/L_{2\mathrm{keV,B}}$ as a function of the average redshift of the stacks. As we can see, the typical difference is 10 or 20% with very weak dependence on redshift. (Linear fitting of $L_{2\mathrm{keV}}/L_{2\mathrm{keV,B}}$ as a function of redshift gives a slope of $-0.12 \pm 0.04$ for RLQs and $0.07 \pm 0.07$ for RQQs. To be consistent with our individual detections, we base our stack analysis as far as possible on $L_{2\mathrm{keV}}$ estimated from the 0.1–2.4 keV band. For the few stacks detected only in the 0.5–2.0 keV band, we use $L_{2\mathrm{keV,B}}$ instead. Table 1 lists the final number of stacks detected in each of our samples.
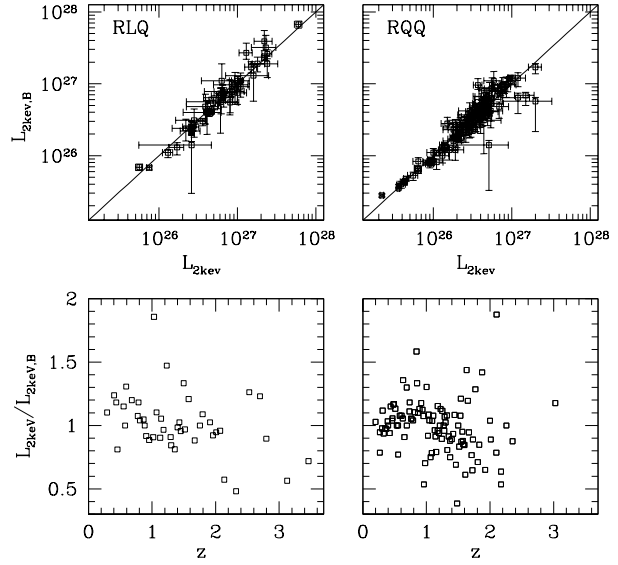
The upper panels of Fig. 7 and Fig. 8 show the average $L_{2\mathrm{keV}}$ of the RQQ and RLQ stacks as a function of their mean $L_{2500}$. Different symbols refer to our different $L_{2500}$ bins and are colour-coded according to redshift. Arrows denote 1-$\sigma$ upper limits for the few stacks we do not detect. Clearly the mean $L_{2\mathrm{keV}}$ values of the stacks correlate extremely well with their mean $L_{2500}$ and the relation between them is well represented by a power law. We fit a linear relation to this plot

$$\log \bar{L}_{2\mathrm{keV}} = \alpha(\log L_{2500} - 30.5) + \delta \tag{9}$$

by minimizing $\chi^2$ weighting each point by an "error" which is the sum in quadrature of two terms, one coming from the observational error in the mean $L_{2\mathrm{keV}}$ measurement for each stack, the other from the expected population variance in the mean for a stack of given size. As we will show in section 4.2.2, the $L_{2\mathrm{keV}}$ values of quasars at given $L_{2500}$ and $z$ follow a log-normal distribution with typical scatter $\sim$ 0.40. Since each of our stacks contains hundreds of sources, the population variance term is smaller than that due to the observational errors. The best-fit linear relations are

$$\log \bar{L}_{2\mathrm{keV}} = (0.68 \pm 0.01)(\log L_{2500} - 30.5) + (26.53 \pm 0.01) \tag{10}$$

for RQQs and

$$\log \bar{L}_{2\mathrm{keV}} = (0.65^{+0.02}_{-0.03})(\log L_{2500} - 30.5) + (26.91^{+0.02}_{-0.01}) \tag{11}$$

for RLQs. These are shown as solid lines in Fig. 7 and Fig. 8 respectively. We also bin the full sample of QSOs into 209 $L_{2500}$ and redshift bins without regard to radio properties,

detecting 199 of them with $L > 7$. The best power-law relation between $\bar{L}_{2\text{keV}}$ and $L_{2500}$ is

$$\log \bar{L}_{2\text{keV}} = (0.64 \pm 0.01)(\log L_{2500} - 30.5) + (26.63 \pm 0.01) \,.\text{(12)}$$

The result for the full sample is thus similar to that for the RQQs, as expected given the relatively small fraction of RLQs in the sample. The uncertainties in the above fits and the corresponding minimum $\chi^2$ values are listed in Table 2.

The relations for RLQs and RQQs have similar slope but the mean X-ray luminosity of RLQs at given $L_{2500}$ is about twice that of RQQs. In the upper panel of Fig. 7, we have over-plotted the mean relation which Strateva et al. (2005) obtained for their complete sample of 228 radio-quiet, non-BAL SDSS AGN with medium-deep ROSAT imaging. More than 80% of these sources have individual X-ray detections. Clearly their results agree well with what we find here for a 100 times larger sample. However, this dramatic increase in sample size (which includes an increase in the number of individual detections by a factor of more than 10) will allow us to make much more precise statements about the $L_{2\text{keV}} - L_{2500}$ distribution than was possible with a sample of 228 objects.

Already in these plots there is some indication for a redshift dependence, especially for the two lowest $L_{2500}$ bins. This is shown more explicitly in the lower panels in Fig. 7 and Fig. 8 where we have divided the mean $L_{2\text{keV}}$ of each stack by the value predicted by the above best-fit relations [equations (10) and (11)] applied to the mean $L_{2500}$ for the stack. We plot the result against the mean redshift of the stack. Although there is no global trend with redshift for either subsample, trends are visible in both cases when one compares symbols of the same type, thus stacks with similar mean $L_{2500}$. These trends are most obvious at low redshift and are stronger for RLQs than for RQQs.

To test explicitly for the significance of this redshift dependence we assume mean X-ray luminosity to vary with redshift as

$$\log L_{2\text{keV}} = \alpha(\log L_{2500} - 30.5) + \beta \log\left(\frac{1+z}{1.5}\right) + \delta \,. \quad (13)$$

The three model parameters $\alpha, \beta$ and $\delta$ can then be estimated by minimizing $\chi^2$ for our sets of stacks. The results, together with the corresponding minimum $\chi^2$ values, are listed in Table 2. Comparing with the values obtained when forcing $\beta = 0$ [i.e. fitting to equation (9)], we see that including a power-law redshift dependence has substantially improved the quality of the fit for the full sample and for the sample of RQQs. For RLQs, however, including a redshift dependence of this form produces little improvement, even though some redshift dependence is evident in the bottom panel of Fig. 8. This is in part because $\chi^2$ per degree of freedom is well below unity for both models for this sample, and in part because the apparent dependence on redshift is poorly described by a single power law. Below we use a more complex model which better describes the apparent behaviour, showing that this leads to a further significant improvement in $\chi^2$ for our stacks of objects in the total and RQQ samples, as well as describing well the joint ($L_{2\text{keV}}$ − $L_{2500}, z$) distribution of individual detections in all three samples.
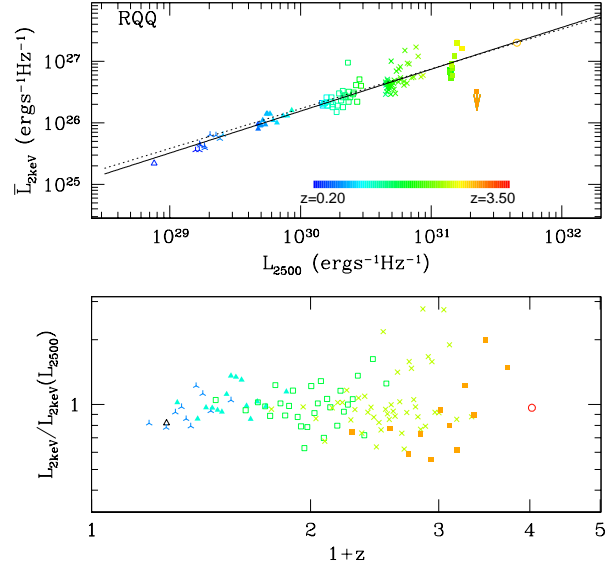


**Figure 7.** Mean X-ray luminosity $L_{2\text{keV}}$ as a function of optical luminosity $L_{2500}$ for RQQs. Symbols in the top row show the mean $L_{2\text{keV}}$ of our stacks of *all* quasars in each redshift and $L_{2500}$ bin, colour-coded according to mean quasar redshift. Solid line is the fitting relation of equation (10). For comparison, the dotted line shows the mean relation between X-ray and optical luminosity given by Strateva et al. (2005). In the bottom row we divide each stack's mean value of $L_{2\text{keV}}$ by the value predicted for its mean $L_{2500}$ by equation (10) and we plot the result against mean redshift. Differing symbols distinguish stacks in our 7 different ranges of $L_{2500}$. Colour-coding here helps to distinguish between symbols of different type.

## 4.2 Results from individual detections alone

The previous section presented results for our subsamples of RLQs and RQQs using stacked data only. Here we consider what can be learned, without using stacks, from our sample of individually detected sources. As mentioned above, we calculate the $L_{2\text{keV}}$ of the individual detected QSOs from their photon count using photon indices $\Gamma = 1.9$ for RLQs and $\Gamma = 2.1$ for RQQs. When we consider the full sample of QSOs without regard to radio properties, we use $\Gamma = 2$. Among our 3206 RLQs there are 341 individual detections after statistical rejection of 36 "contaminants". Among our 25689 RQQs there are 2163 detections left after rejection of 130 "contaminants". When the full sample of 46420 DR3 quasars is analysed there are 3120 detections after rejection of 246 "contaminants". These detection statistics are listed for each sample in Table 1.

### 4.2.1 The redshift dependence

In Section 4.1, we showed evidence that the average X-ray luminosity of quasars of given $L_{2500}$ depends on redshift both for RLQs and for RQQs. In this section, we use data from our individual detections to further check and quantify this dependence.

In the bottom panels of Fig. 7 and 8, the $L_{2\text{keV}}$ dependence on redshift is more evident at low redshifts than that
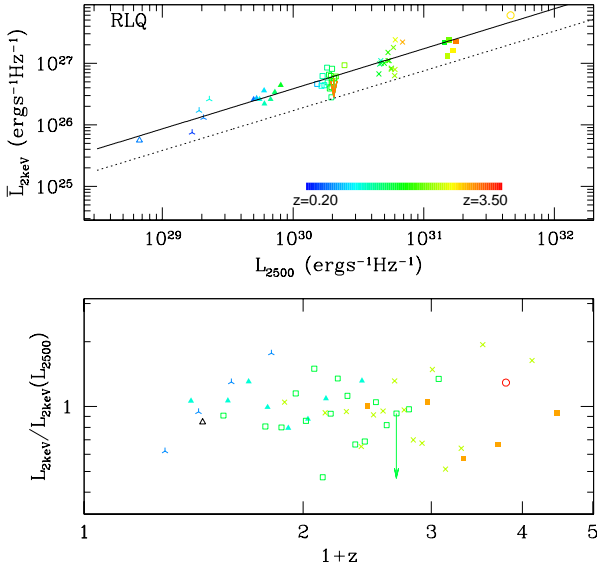
**Figure 8.** Mean X-ray luminosity $L_{2\mathrm{keV}}$ as a function of mean optical luminosity $L_{2500}$ and redshift for stacks of RLQs. The structure of the figure is the same as that of Fig. 7. The dotted line again gives the relation of Strateva et al. (2005).

at high for both classes of quasar. Based on this impression, we parameterize the average $L_{2\mathrm{keV}}$ of quasars of given $L_{2500}$ and $z$ through

$$\log L_{2\mathrm{keV}} =$$
$$\begin{cases} \alpha(\log L_{2500} - 30.5) + \beta \log\left(\frac{1+z}{1+z_0}\right) + \delta & \text{for } (z < z_0) \\ \alpha(\log L_{2500} - 30.5) + \gamma \log\left(\frac{1+z}{1+z_0}\right) + \delta & \text{for } (z > z_0) \end{cases} \quad (14)$$

With this assumption, the average $L_{2\mathrm{keV}}$ is proportional to $(1+z)^{\beta}$ at $z < z_0$ and proportional to $(1+z)^{\gamma}$ at $z > z_0$ but is proportional to $L_{2500}^{\alpha}$ at all redshifts. For $\beta \approx \gamma$, this relation is equivalent to equation (13).

As we will verify in Section 4.2.2, the distribution of $L_{2\mathrm{keV}}$ at given $L_{2500}$ and $z$ is well approximated by a log-normal with scatter $\sim 0.40$, almost independent of $L_{2500}$ and $z$. Adopting this model, the likelihood that the $i$th SDSS quasar will be detected with X-ray luminosity $L_{2\mathrm{keV},i}$ is

$$P_i = f(L_{2\mathrm{keV},i} | L_{2500,i}, z_i) \quad (15)$$

where $f$ is the log-normal density function with median given in terms of $L_{2500}$ and $z$ by equation (14) and with scatter $\sim 0.40$ [see equation (19)]. As shown in Section 3.2, we can calculate the minimum detectable X-ray flux for a QSO from its position, based on local values of Galactic hydrogen column, RASS effective exposure time and RASS background level. Given the quasar's redshift, we can convert this minimum flux to a minimum detectable X-ray luminosity $L_{\min}$. Thus for each undetected DR3 quasar, we know $L_{2\mathrm{keV}} < L_{\min}$. The likelihood of each non-detections can then be defined as

$$P_{non,j} = \int_{-\infty}^{L_{\min,j}} f(L_{2\mathrm{keV}} | L_{2500,j}, z_j) dL_{2\mathrm{keV}}. \quad (16)$$

For each set of parameters $\alpha, \beta, \gamma, \delta, z_0$ in equation (14),

the joint likelihood of $N$ individual detections and $M$ non-detections can be written as

$$\mathcal{L} \propto \prod_{i=1,N} P_i \prod_{j=1,M} P_{non,j} \quad (17)$$

The 5 model parameters then can be estimated by maximizing $\mathcal{L}$. For sufficiently large samples (such as those used here) the quantity $2\ln(\mathcal{L}_{\max}/\mathcal{L})$ is distributed like $\chi^2$ with 3 degrees of freedom. By marginalizing over some of the parameters we can construct confidence regions for the other parameters in the standard way. For comparison, we also use $\chi^2$ statistics to estimate the model parameters in equation (13) using the mean $L_{2\mathrm{keV}}$, $L_{2500}$ and $z$ of the stacks of all RQQ's and of all quasars analysed in Section 4.1, together with the $L_{2\mathrm{keV}}$ errors estimated there. The number of RLQ stacks is too few to get meaningful estimates for this many parameters.

We show maximum likelihood estimates and confidence contours with solid lines for two pairs of model parameters in Fig. 9. Results from $\chi^2$ fitting of the stacks are represented by dotted contours. Model parameter estimates from the two techniques are also listed in Tables 3 and 2 respectively. The minimum $\chi^2$ values listed in Table 2 show that this more complex model for the redshift dependence fits the mean $L_{2\mathrm{keV}}$ of our stacks significantly better than the simple power-law model of equation (13). We note that the $\chi^2$ values for RQQs are still significantly larger than the number of degrees of freedom in fitting equation (14). This is caused by several "outliers" with small weighted errors, each contributing $\Delta\chi^2 > 10$ in the fitting. However, the inclusion or exclusion of these "outliers" does not change any of our fitting results.

The top panels of Fig. 9 show that for our full set of quasars the parameters of equation (14) are all well constrained. In addition, the values obtained from the individual detections agree very well with those obtained from the "total" stacks. Evolution is clearly detected in the sense that the typical $L_{2\mathrm{keV}}$ associated with quasars of given $L_{2500}$ increases with redshift (both $\beta$ and $\gamma$ are significantly greater than zero). This evolution is substantially stronger at low redshift than at high ($\beta > \gamma$) and the transition redshift $z_0 \sim 0.5$ is well determined. The $L_{2\mathrm{keV}} - L_{2500}$ relation is significantly shallower than found above when fitting the "total" stacks without allowing for the redshift dependence: $\alpha = 0.51$ here as opposed to $\alpha = 0.64$ in equation (12). This is a result of the strong selection-induced correlation between $L_{2500}$ and redshift which is present in all our samples.

For radio-loud quasars (bottom panels of Fig. 9) the maximum likelihood analysis gives parameters which, with one exception, are consistent at about the 1-$\sigma$ level or better with those obtained for the sample as a whole. The exception is the overall normalisation; as before we find that the RLQs are systematically brighter in soft X-rays than the population as a whole by about a factor of 2. The constraints on $\beta$ are relatively poor for RLQs. The maximum likelihood value $\beta = 3.4$ is substantially larger than that for the sample as a whole ($\beta = 1.8$) suggesting that radio quasars may evolve more strongly than typical quasars at low $z$, but the difference is not statistically significant. The "total" stacks for RLQs are fully consistent with these parameters but do not contain enough information to constrain them significantly.
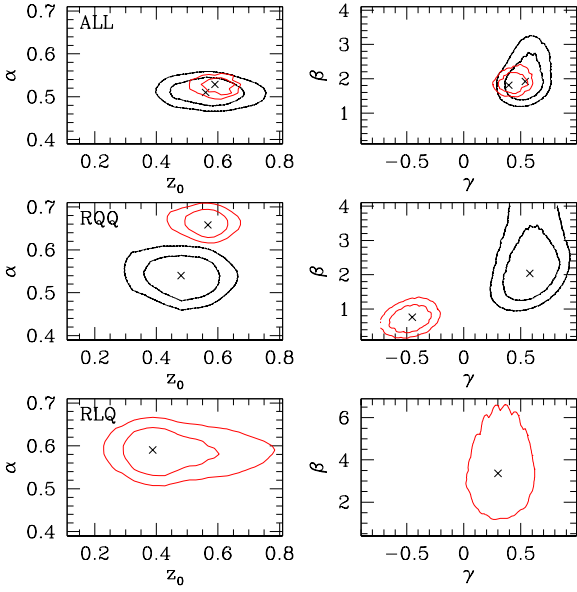
**Figure 9.** Maximum likelihood estimates and confidence contours for model parameters in equations (14). Results for the full QSO sample, RQQs and RLQs are shown in the first, second and third rows respectively. Solid contours show 68.3% and 90% confidence level contours obtained from the maximum likelihood analysis of individual detections in Section 4.2.1, while dashed contours give similar contours based on $\chi^2$ fitting of the "total" stacks in Section 4.1. Where only one contour is given it is the 68.3% confidence level contour.

The situation for radio-quiet quasars (middle panels of Fig. 9) is more complex. The parameter estimates we obtain from the "total" stacks are very similar to those found for the quasar sample as a whole (and also to those found for RLQs). This is expected since about 90% of AGN as a whole are radio quiet. The parameter estimates we obtain from the individual RQQ detections are, however, consistent neither with those obtained from the "total" RQQ stacks nor with those found for the other two samples. Substantially weaker evolution is indicated ($\beta$ and $\gamma$ are both much smaller) and, to compensate, the slope found for the $L_{2\mathrm{keV}} - L_{2500}$ relation is steeper. Clearly the two sets of results for the RQQs cannot both be correct, and it seems suspicious that the RQQ behaviour should differ substantially from that of the sample as a whole. For these reasons, and also because the "total" stacks use our dataset as a whole and extend out to $z \sim 4$ whereas there are very few individual RQQ detections at $z > 2$, we adopt the parameters obtained from the RQQ "total" stacks as those best representing the population. We present independent evidence below (Section 4.3 and Fig. 12) that this is indeed the correct choice.

### 4.2.2   The distribution of $L_{2\mathrm{keV}}$

In the last section, we assumed the distribution of $L_{2\mathrm{keV}}$ at given $L_{2500}$ and $z$ to be log-normal with logarithmic dispersion $\sim 0.40$ and we used maximum likelihood techniques to estimate its median value as a function of $L_{2500}$ and $z$. In this

section, we check the log-normal and nearly constant scatter assumptions directly against our individual detection data.

For simplicity, we here correct for redshift evolution using the results of the last section, and we study how the distribution of redshift-corrected $L_{2\mathrm{keV}}$ values depends on $L_{2500}$. Specifically, we correct the X-ray luminosity of each individually detected quasar to redshift $z_0$ using equation (14) with the maximum likelihood parameters of Table 3. For RQQs, we make this correction by using the $\chi^2$ parameter estimates listed in Table 2. We denote the result by $L_{2\mathrm{keV},z_0}$. While we assume the redshift dependence deduced in subsection 4.2.1 throughout the current section, we assumed the value of the scatter deduced below when estimating this redshift dependence in Section 4.2.1. The results of the two sections are, in fact, consistent and were derived by iteration.

We divide the individual detections into the same 7 $L_{2500}$ bins that we used in Section 4.1 for stacks. The fraction of the quasars in each $L_{2500}$ range which are individually detectable in the RASS at given $L_{2\mathrm{keV}}$ depends on their redshifts and on the RASS detection sensitivity at their positions. We use the the minimum luminosities $L_{\mathrm{min},j}$ of Section 4.2.1 to calculate these fractions at each $L_{2\mathrm{keV}}$. They can then be used to correct the observed distribution of $L_{2\mathrm{keV}}$ for the effects of the RASS flux limit and thus to estimate the unconstrained distribution of $L_{2\mathrm{keV}}$ for quasars in the chosen $L_{2500}$ range. Each detected quasar is simply weighted with a factor $1/F_i$, where $F_i$ is defined by

$$F_i = \frac{N(L_{\mathrm{min}} < L_i)}{N_{tot}}. \tag{18}$$

Here $N_{tot}$ is the *total* number of quasars in the $L_{2500}$ bin (including non-detections and "contaminants") and $N(L_{\mathrm{min}} < L_i)$ is the number of these for which the minimum detectable $L_{2\mathrm{keV}}$ is less than the X-ray luminosity $L_i$ of the particular detected quasar under consideration.

In Fig. 10, we show the resulting luminosity distributions in histogram form for the individually detected RQQs in each $L_{2500}$ bin, together with the original un-weighted histograms of $L_{2\mathrm{keV}}$. After correction, the sampled part of the luminosity distribution is well represented by a log-normal in all cases. We do not show the histograms for RLQs, which are similar but more noisy as a result of the limited number of individual detections. Histograms for all detections, independent of radio properties, are very similar to those shown here for the RQQs.

Based on these results we now *assume* the distribution of evolution-corrected $L_{2\mathrm{keV}}$ at given $L_{2500}$ to be log-normal,

$$P(L_{2\mathrm{keV},z_0}|L_{2500}) = \frac{1}{\sqrt{2\pi}\sigma_{L_{2\mathrm{keV}}}} \exp\left[-\frac{\log\left(L_{2\mathrm{keV},z_0}/\tilde{L}_{2\mathrm{keV},z_0}\right)^2}{2\sigma_{L_{2\mathrm{keV}}}^2}\right], \tag{19}$$

and we use the maximum likelihood method of Section 4.2.1 to estimate the two parameters $\tilde{L}_{2\mathrm{keV},z_0}$ and $\sigma_{L_{2\mathrm{keV}}}$ (the median and the logarithmic dispersion) for each $L_{2500}$ bin. The resulting best-fit log-normal distributions are shown as dotted curves in each $L_{2500}$ panel of Fig. 10. They clearly agree very well with the directly estimated $L_{2\mathrm{keV},z_0}$ distributions.

Fig. 11 shows these maximum likelihood estimates of the median and scatter as functions of $L_{2500}$, with open triangles and open squares denoting RLQs and RQQs respectively. Error bars indicate 90 percent confidence intervals. The median value of $\log L_{2\mathrm{keV},z_0}$ increases linearly with $\log \bar{L}_{2500}$ both for RLQs and for RQQs. The relation for
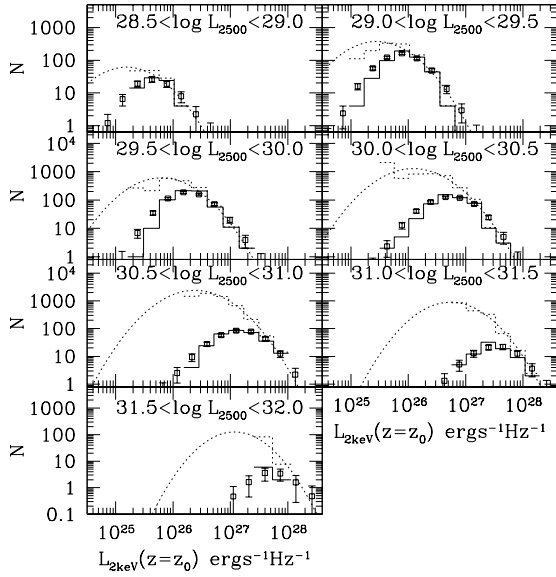
**Figure 10.** The distribution of $L_{2\mathrm{keV}}$ for RQQs of given $L_{2500}$. Each panel refers to a different range of $L_{2500}$ as indicated. Solid histograms show the directly observed counts of detected quasars as a function of $L_{2\mathrm{keV}}$. The dotted histograms show the result of weighting each quasar by the inverse of the fraction of the (sub)sample in which its luminosity could have been detected. This produces an estimate of the true X-ray luminosity distribution in each $L_{2500}$ bin (see text for details). Maximum likelihood log-normal fits to the distributions of individual detections are plotted as dotted curves. The distributions of individual detections predicted from these log-normal fits are shown as squares with error bars to denote the scatter among individual Monte Carlo realizations of the luminosities predicted for the quasars in each $L_{2500}$ range.

RLQs shows a steeper slope and is systematically higher than that for RQQs Least squares fits to these data give

$$\log \tilde{L}_{2\mathrm{keV},z_0} = (0.62 \pm 0.06)(\log L_{2500} - 30.5) + (26.55 \pm 0.04)$$
$$\sigma_{L_{2\mathrm{keV}}} = (-0.03 \pm 0.04)(\log L_{2500} - 30.5) + (0.40 \pm 0.02) \quad (20)$$

for RLQs and

$$\log \tilde{L}_{2\mathrm{keV},z_0} = (0.53 \pm 0.02)(\log L_{2500} - 30.5) + (26.18 \pm 0.02)$$
$$\sigma_{L_{2\mathrm{keV}}} = (-0.04 \pm 0.01)(\log L_{2500} - 30.5) + (0.40 \pm 0.01) \quad (21)$$

for RQQs. Fitting to the full sample of QSOs gives

$$\log \tilde{L}_{2\mathrm{keV},z_0} = (0.54 \pm 0.01)(\log L_{2500} - 30.5) + (26.29 \pm 0.01)$$
$$\sigma_{L_{2\mathrm{keV}}} = (-0.04 \pm 0.01)(\log L_{2500} - 30.5) + (0.42 \pm 0.01) \quad (22)$$

The fits to RLQs and RQQs are plotted as solid straight lines in Fig. 11 and clearly represent the data very well. Furthermore they are consistent both with our fits to the stacked data [equations (11) and (10) and Fig. 7 and 8; note that one must correct for the offset between median and mean] and with the joint fits of equation (14) for which parameters are given in Table 2 and 3. We detect no significant dependence of the scatter of the $L_{2\mathrm{keV}}$ distribution on $L_{2500}$ and obtain a value consistent with 0.40 (as assumed in Section 4.2.1) in all cases.

The parameter estimates of this section do not use any information about the X-ray luminosities of individually un-
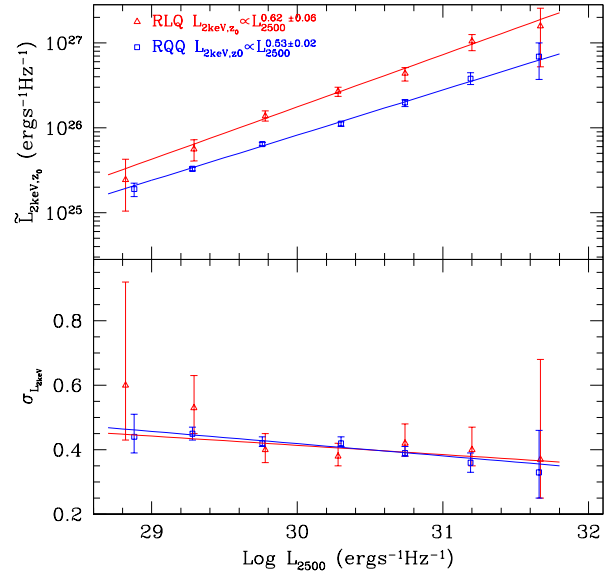


**Figure 11.** The evolution-corrected X-ray luminosity distribution of quasars as a function of $L_{2500}$. The median (upper panel) and the logarithmic scatter (lower panel) of a log-normal fit to the evolution-corrected $L_{2\mathrm{keV},z_0}$ distribution are shown separately for RLQs (open triangles) and for RQQs (open squares). Error-bars denote 90% confidence intervals. The $L_{2500}$ values for the squares are shifted slightly for clarity. These estimates are based on individual detections only. The solid lines show least-squares error-weighted fits to the points [equations (20) and (21)].

detected quasars. Mean values of these luminosities can, however, be measured by stacking. We now carry out such stacking in order to check for consistency with the above results.

### 4.3 Luminosities for stacks of undetected quasars

The results of the last section show that although the high X-ray luminosity part of the distribution of $L_{2\mathrm{keV},z_0}$ is well described by a log-normal function, the shape of the distribution below the median X-ray luminosity is not constrained by our individual detections. In this section, we use stacking analysis to study the mean X-ray luminosity of individually undetected sources, comparing our measurements with predictions from the log-normal models of the last section.

The undetected sources were split into seven ranges of $L_{2500}$ and then within each range they were separated into a series of bins according to redshift. The ranges of $L_{2500}$ and redshift are the same as those of the "total" stacks in Section 4.1. For the 51 stacks of RLQs and 118 stacks of RQQs, the numbers of detections with $L > 7$ (in either the 0.1–2.4 keV or the 0.5–2.0 keV band) are 49 and 117 respectively.

We use Monte-Carlo simulation to check whether the X-ray luminosities of these stacks are consistent with the $L_{2\mathrm{keV}}$ distributions we have fit to the individual detections alone. To do this, we randomly generate a value of $L_{2\mathrm{keV},z_0}$ for each real quasar using a log-normal distribution with median and scatter given by the symbols in Fig. 11. After undoing the evolution corrections using equation (14), we get a simulated

$L_{2\text{keV}}$ for each quasar. These Monte Carlo luminosities are then converted into X-ray fluxes in the $0.1 - 2.4\,\text{keV}$ band based on the quasar redshifts and an assumed photon index $\Gamma$. As before, we take $\Gamma = 1.9$ for RLQs and $\Gamma = 2.1$ for RQQs. Using the RASS detection completeness function $C_{\text{RASS}}(f)$ described in Section 3.2, we find the probability that each source would be individually detected by the RASS. Based on Monte-Carlo sampling with this probability, we pick sources as "individual RASS detections". Undetected quasars are then placed into the same redshift bins as the real data and we simulate the stacking process using equations (7) and (8). These procedures produce both individual and stacked detections for a simulated sample with the chosen log-normal X-ray luminosity distribution. We repeat this simulation 200 times and use the mean and scatter among the 200 realizations to determine our model expectation and its variance both for individual and for stacked detections.

In Fig. 12 we compare the average X-ray luminosity of the simulated stacks with the real data for RQQs. The figures for RLQs and for the quasar sample as a whole show equally good agreement and are not given here. For each $L_{2500}$ bin, we show the mean $L_{2\text{keV}}$ of stacks as function of mean redshift. The observations are shown as triangles with error bars giving the 1-$\sigma$ uncertainties in the measured flux. Model expectations based on the parameter set obtained from the "total" stacks (Table 2) are shown by connected solid lines except in the lowest and highest $L_{2500}$ bins which only have one stack. Note that the variance of the model predictions is much smaller than the observational errors as shown explicitly in the lowest and highest $L_{2500}$ panels. A similar prediction based on the parameters found from our likelihood analysis of individual RQQ detections (Table 3) is shown by a dashed line. It is clear that the prediction based on parameters from the "total" stacks is in excellent agreement with these independent data, whereas that based on the maximum likelihood analysis fits poorly at the higher redshifts. This provides further support both for evolution parameters based on the "total' stacks and for our log-normal model for the X-ray luminosity distribution, reinforcing the fact that the incompleteness-corrected $L_{2\text{keV}}$ distributions of Fig. 10 have log-normal shape on the bright side of the peak.

As a by-product from these Monte-Carlo simulations, Fig. 10 shows model predictions for the distribution of $L_{2\text{keV},z_0}$ for individual detections. These are plotted as open squares with error bars representing the scatter among the 200 simulations. These symbols should be compared with the solid histograms which show number counts for individual detections in the real data. Again there is good agreement, demonstrating the consistency of our models and our completeness corrections.

### 4.4    $L_{2\text{keV}}$ versus [OIII] line luminosity

In this section, we use [OIII]$\lambda 5007$ line luminosity, $L_{\text{[OIII]}}$, instead of $L_{2500}$ to characterize the strength of quasar activity. As we have mentioned before, only the 9103 lowest redshift quasars ($z < 0.8$) have measurements of [OIII]$\lambda 5007$ line strength. Among them, there are 587 RLQs and 5880 RQQs. The distributions of $L_{\text{[OIII]}}$ were shown as histograms in the lower panels of Fig. 2. For RLQs, the number of in-
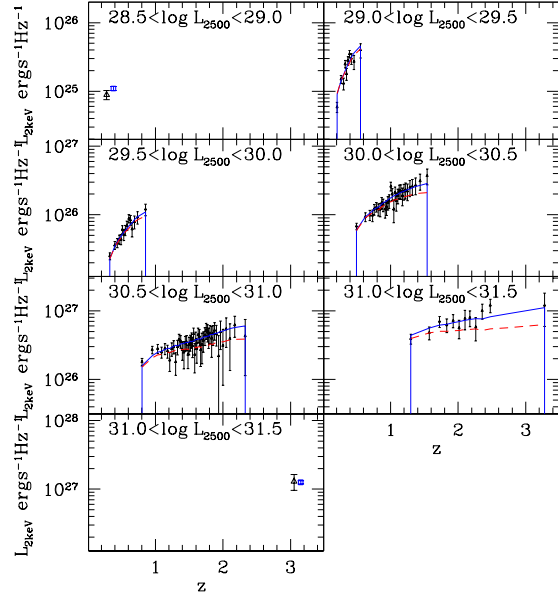


**Figure 12.** The mean $L_{2\text{keV}}$ of stacks of non-detected RQQs are compared to predictions from the log-normal models fitted to individually detected RQQs and to "total" stacks of RQQs. Within each $L_{2500}$ bin the mean $L_{2\text{keV}}$ of each stack is plotted as a triangle with an error bar representing its 1-$\sigma$ observational uncertainty. The values predicted for these stacks by the log-normal models are indicated by continuous solid lines for the model fit to the "total" stacks, and by dashed lines for the model fit to the individual detections. Clearly the former model is consistent with these independent data, while the latter is not.

dividual RASS detections is 190 and the number of random "contaminants" is about 9. For RQQs, these two numbers are 1532 and 23.

As for $L_{2500}$, we first stack the QSOs and study mean $L_{2\text{keV}}$ as a function of $L_{\text{[OIII]}}$ and redshift. We divide objects into 6 $L_{\text{[OIII]}}$ bins and stack them according to exposure time and rank in redshift. We choose the total exposure time of a stack of RLQs to be $\sim 10$ ks and of a stack of RQQs to be $\sim 30$ ks. This gives 26 stacks of RLQs and 90 stacks of RQQs. For the full sample, regardless of radio properties, this gives 109 stacks. All stacks have RASS detections with $L > 7$, except for the stack of RLQs with the lowest $L_{\text{[OIII]}}$ which contains only 3 QSOs.

In Fig. 13 (upper panels) we show the mean $L_{2\text{keV}}$ of these "total" stacks as function of $L_{\text{[OIII]}}$ for both RLQs and RQQs. Symbols are colour-coded according to mean redshift. At given $L_{\text{[OIII]}}$, RLQs again have larger $L_{2\text{keV}}$ than RQQs. For RQQs, there is a very clear trend with redshift in all the $L_{\text{[OIII]}}$ bins. Higher redshift RQQs have higher mean $L_{2\text{keV}}$ values. To quantify this redshift dependence, we apply the $\chi^2$ fitting techniques of Section 4.1 to these stacks and the maximum likelihood methods of Section 4.2.1 to the individual detections.

We again assume the distribution of $L_{2\text{keV}}$ at given $L_{\text{[OIII]}}$ and $z$ to be log-normal with logarithmic dispersion $\sim 0.45$ (see Fig. 15). We model the dependence of the median $L_{2\text{keV}}$ on the $L_{\text{[OIII]}}$ and $z$ by

$$\log \tilde{L}_{2\text{keV}} = \alpha(\log L_{\text{[OIII]}} - 8.5) + \beta \log(1 + z) + \delta \qquad (23)$$
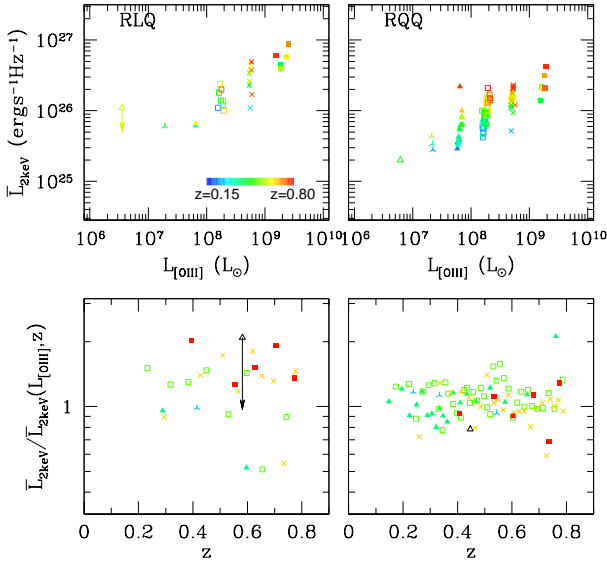
**Figure 13.** $L_{2\mathrm{keV}}$ as a function of $L_{\mathrm{[OIII]}}$. The left panels show results for RLQs and the right panels for RQQs. In each panel mean $L_{2\mathrm{keV}}$ is plotted as a function of mean $L_{\mathrm{[OIII]}}$ for stacks of all quasars in a series of bins which are colour-coded according to their mean redshift. In the bottom two panels, we divide each stack's mean $L_{2\mathrm{keV}}$ by the value predicted for its mean $L_{\mathrm{[OIII]}}$ and $z$ by equation (23), and we plot this ratio against mean redshift. Different symbol types and colours here distinguish quasars in the different $L_{\mathrm{[OIII]}}$ bins.

Maximum likelihood estimates of model parameters are then obtained from our individual detections as in Section 4.2.1. We show estimates of $\alpha$ and $\beta$ together with their confidence contours in Fig. 14 for the RLQ and RQQ subsamples. Parameter estimates for these two subsamples and for the full sample of quasars with [OIII]$\lambda$5007 are also listed in Table 3. The values of $\alpha$ for the two samples differ at the 1-$\sigma$ level while the values of $\beta$ are almost identical. Interestingly, the values of both parameters are quite different from those we found above when characterising the optical luminosity of quasars by $L_{2500}$. The optical luminosity dependence is weaker but the redshift dependence is stronger. In addition, the differences between RLQs and RQQs are smaller and are not significant. The $1-\sigma$ confidence region for RLQ model parameters is, however, quite large. In the bottom two panels of Fig. 13, we divide the mean $L_{2\mathrm{keV}}$ of the "total" stacks by the values predicted by equation (23) (correcting for the difference between mean and median) at their mean $L_{\mathrm{[OIII]}}$ and $z$. The resulting ratios are plotted against mean $z$. Clearly the evolution inferred from our analysis of individual detections does a very good job of removing systematic redshift dependences from the "total" stacks also.

A $\chi^2$ analysis of the stacked data similar to that of Section 4.1 gives consistent conclusions. Fitting equation (23) to the mean $L_{2\mathrm{keV}}$, $L_{\mathrm{[OIII]}}$ and $z$ values of the stacks shown in Fig. 13 produces the parameter estimates listed in Table 2. These agree well with those derived from maximum likelihood fits to the individual detections(Table 3) and again the redshift dependence is detected at very high significance.
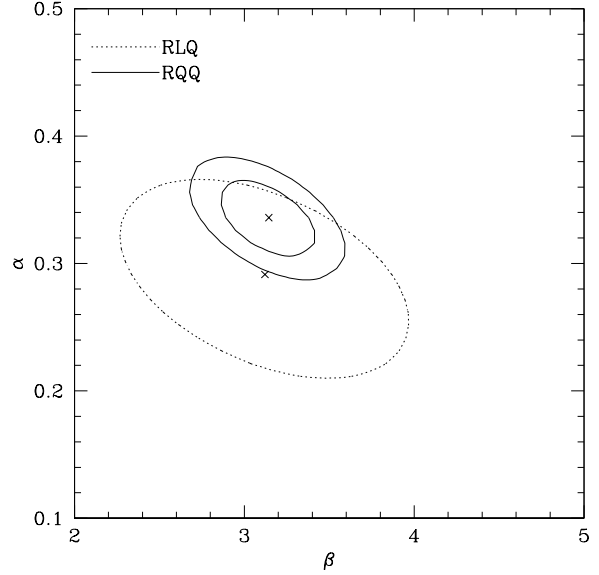


**Figure 14.** Maximum likelihood estimates of the model parameters $\alpha$ and $\beta$ in equation (23) for RLQs and for RQQs. Solid lines show the 1- and $2-\sigma$ confidence contours for RQQs whereas the dotted line shows the 1-$\sigma$ confidence contour for RLQs.

This is perhaps best seen by comparing with the results of $\chi^2$ fitting to a simple, redshift-independent power-law relation

$$\log \tilde{L}_{2\mathrm{keV}} = \alpha(\log L_{\mathrm{[OIII]}} - 8.5) + \delta \qquad (24)$$

The results given in Table 2 show once more that substantially larger values of $\alpha$ are inferred if the redshift dependence is ignored, but, more importantly, the much larger minimum $\chi^2$ values found for all three samples when forcing $\beta = 0$ demonstrate that a strong redshift dependence really is required by the data.

The power-law redshift dependence we assume here is similar to that of equation (13) rather than to the more complex parametrisation of equation (14) which we preferred above when analysing soft X-ray properties as a function of $L_{2500}$. This choice reflects both the limited redshift range of QSOs with measured [OIII]$\lambda$5007 ($z < 0.8$), and the smaller samples analysed here, which do not justify the inclusion of two additional model parameters.

With the redshift dependence derived above, we "correct" all X-ray luminosities to $z = 0$ in order to study the dependence of $L_{2\mathrm{keV},z=0}$ on $L_{\mathrm{[OIII]}}$ in more detail. We divide the QSOs into six $L_{\mathrm{[OIII]}}$ bins with varying width and assume that the $L_{2\mathrm{keV},z=0}$ values for QSOs in each bin are distributed log-normally. We then use the maximum likelihood method of Section 4.2.2 to estimate the median and logarithmic dispersion of this distribution. We show the results as functions of $L_{\mathrm{[OIII]}}$ in Fig. 15. A simple error-weighted least-squares fit gives

$$\log \tilde{L}_{2\mathrm{keV},z=0} = (0.29 \pm 0.11)(\log L_{\mathrm{[OIII]}} - 8.5) + (25.44 \pm 0.06)$$
$$\sigma_{L_{2\mathrm{keV}}} = (0.02 \pm 0.09)(\log L_{\mathrm{[OIII]}} - 8.5) + (0.48 \pm 0.05) \quad (25)$$

for RLQs and

$$\log \tilde{L}_{2\mathrm{keV},z=0} = (0.33 \pm 0.03)(\log L_{\mathrm{[OIII]}} - 8.5) + (25.24 \pm 0.02)$$
$$\sigma_{L_{2\mathrm{keV}}} = (-0.01 \pm 0.03)(\log L_{\mathrm{[OIII]}} - 8.5) + (0.45 \pm 0.01) \quad (26)$$

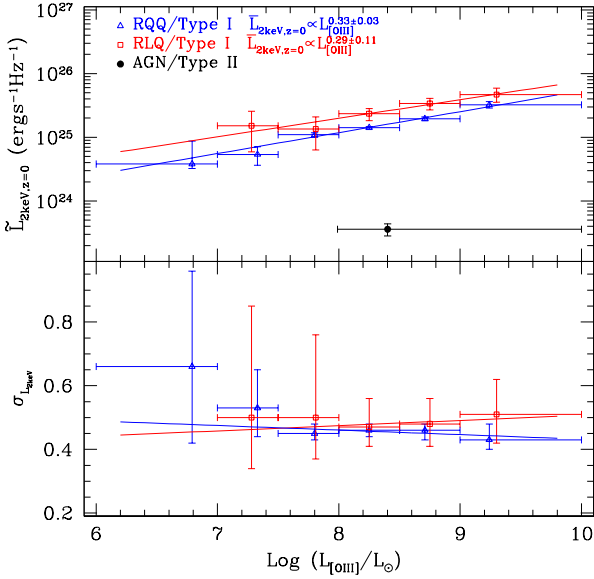**Figure 15.** The median and scatter of the evolution-corrected Ł$_{2keV,z=0}$ distribution at fixed $L_{[OIII]}$. Horizontal error-bars indicate the range of the $L_{[OIII]}$ bins while vertical error-bars indicate 90 percent confidence intervals. Points are plotted at the mean $\log L_{[OIII]}$ of the quasars in each bin. Triangles and squares show results for RLQs and RQQs respectively, whereas the filled circle represents the mean $L_{2keV}$ value measured for type II AGN (see Section 4.5). Solid lines are the least-squares fits of equations (25) and (26).

for RQQs and

$$\log \tilde{L}_{2keV,z=0} = (0.33 \pm 0.03)(\log L_{[OIII]} - 8.5) + (25.33 \pm 0.02)$$
$$\sigma_{L_{2keV}} = (-0.01 \pm 0.02)(\log L_{[OIII]} - 8.5) + (0.43 \pm 0.01) \quad (27)$$

for the full sample.

All three samples have similar power law indices and a much shallower $L_{2keV,z=0} - L_{[OIII]}$ relation than the $L_{2keV,z_0} - L_{2500}$ relation we found earlier. The typical $L_{2keV,z=0}$ of RLQs is about 1.6 times larger than that of RQQs at given $L_{[OIII]}$, slightly smaller than the factor of 2 we found for the $L_{2500}$ case. This is because RLQs have higher $L_{[OIII]}$ than RQQs with similar $L_{2500}$ (see Fig. 2). It is also interesting to note that the dispersion in the $L_{2keV}$ distribution is $\sim 0.45$ almost independent of luminosity, slightly higher than that we found for the $L_{2500}$ case in Section 4.2.2. Moreover, all the results here are consistent with our maximum likelihood estimates of the model parameters in equation (23) (see Table 3).

## 4.5 Type II AGN

As mentioned earlier, the DR3 quasar catalogue includes only type I quasars. For comparison, we now study the properties of a sample of type II AGN. This is a set of 22623 narrow-line type II AGN selected from the SDSS main sample of galaxies with $0.02 < z < 0.3$ (Kauffmann et al. 2003). The [OIII]$\lambda$5007 luminosity of each AGN was measured and used to characterize its nuclear activity.

Applying our maximum likelihood X-ray detection pro-

cedure to these objects gives only 211 individual detections with $L \geq 7$. These detections are significantly biased towards objects with high $L_{[OIII]}$. The number of spurious detections is about 104, as estimated from a sample of random positions with the same sky structure. The very low fraction of individual detections and high fraction of contaminants suggest that the soft X-ray emission of type II AGN is very weak. Thus, it is difficult to carry out the same analysis as for type I quasars. Instead, we stack all the candidates to derive their average X-ray fluxes. We first divide the type II AGN into ten bins of $L_{[OIII]}$, each containing the same number of objects. For each $L_{[OIII]}$ bin, we combine all the AGN into one stack. For these ten stacks, we obtain only one detection with $L \geq 7$ (for the bin with the highest $L_{[OIII]}$). We calculate the weighted average of the X-ray luminosity $L_{2keV}$ from equation (8) for this $L_{[OIII]}$ bin. The result is shown as the filled circle in Fig. 15. The mean X-ray luminosity of type II AGN is about 75 times smaller than the median luminosity of type I radio-quiet AGN with similar [OIII] line luminosity and redshift. (The average redshift of the type II AGN in this bin is about 0.14.) Since the mean X-ray luminosity of the type I AGN is about a factor of 2 larger than their median X-ray luminosity, the effective shift in the $L_{2keV}$ distribution between the two populations is probably about a factor of 150.

## 5 DISCUSSION AND CONCLUSIONS

In this paper, we have studied the soft X-ray properties of quasars based on the SDSS DR3 quasar catalogue and the RASS. The FIRST catalogue enabled us to define subsamples of radio-loud and radio-quiet objects. We used both individual and stack detections to investigate the X-ray properties of quasars as a function of $L_{2500}$, of radio power, of $z$ and of $L_{[OIII]}$.

By stacking all QSOs with similar optical luminosity and redshift, we have shown that the average $L_{2keV}$ of both RLQs and RQQs depends significantly on redshift at given optical luminosity. At fixed UV continuum luminosity $L_{2500}$ and at low redshift ($z < 0.5$) the RLQ population may evolve more strongly than the RQQs. At higher redshift, the X-ray brightening of RLQs and RQQs of given $L_{2500}$ are both considerably slower. If [OIII] line luminosity $L_{[OIII]}$ is substituted for $L_{2500}$, then RLQs and RQQs show similar and strong evolution out to $z = 0.8$. Assuming that the redshift and optical luminosity dependences of the $L_{2keV}$ distribution separate, we correct all X-ray luminosities to a fiducial redshift and analyse in more detail the shape of the distribution of the evolution-corrected X-ray luminosity $\log L_{2keV,z_0}$ at given optical luminosity. This distribution is well approximated by a log-normal, at least for quasars more X-ray bright than the median. Adopting this model we find a tight but nonlinear relation between $\tilde{L}_{2keV}$ and optical luminosity ($L_{2500}$ or $L_{[OIII]}$). The dispersion in $\log L_{2keV}$ is roughly $\sim 0.40$, independent of optical luminosity. The typical X-ray luminosity of RLQs is twice that of RQQs of the same $L_{2500}$, and 1.6 times that of RQQs of the same $L_{[OIII]}$. In addition, we find the average soft X-ray emission of type II AGN to be more than 100 times weaker than that of radio-quiet type I quasars of the same $L_{[OIII]}$ and redshift.

Many of our results have been seen in previous stud-

ies. For example, the nonlinear relation between $L_{2\mathrm{keV}}$ and $L_{2500}$ is consistent with that of Vignali, Brandt & Schneider (2003a); the result that RLQs have stronger soft X-ray emission than RQQs is consistent with that of Brinkmann et al. (2000); the result that soft X-ray emission from type II AGN is very weak is consistent with that of Zakamska et al. (2004). There are also a number of new results, for example, that $\alpha_{OX}$ depends not only on optical luminosity but also on redshift. At given optical luminosity $L_{2500}$, the typical value of $\alpha_{OX}$ decreases by about 0.3 from $z \approx 0$ to $z \approx 5$ [extrapolated from our best fits to equation (14)] both for RLQs and for RQQs. This is significant compared to earlier claims for the redshift independence of $\alpha_{OX}$. For example, Strateva et al. (2005) quote $\Delta\alpha_{OX} \approx 0.03$ from $z \approx 0$ to 5. The apparent change in redshift dependence around $z \sim 0.5$ is very interesting. We note that rest-frame 2500Å passes out of the SDSS spectral range at about this redshift. We obtain the 2500Å flux for such low redshift quasars by extrapolation using the Vanden Berk et al. (2001) composite quasar spectrum, a procedure which could plausibly introduce systematic biases into $L_{2500}$. To check for such effects, we repeated our analysis replacing $L_{2500}$ by $L_{3500}$, the continuum luminosity at rest-frame 3500Å. This can be estimated directly from the SDSS spectrum for all our quasars with $z < 1.63$. This substitution did not alter any of our conclusions about low-redshift evolution either for RLQs or for RQQs. Another possible systematic might arise from host-galaxy contributions to $L_{2500}$ in low-redshift ($z < 0.5$) and low-luminosity quasars. Strateva et al. (2005) addressed this issue in their own study, concluding that the host-galaxy contribution does not exceed 20 percent.

The most detailed previous study of the relation between $L_{2\mathrm{keV}}$ and $L_{2500}$ is that of Strateva et al. (2005), based on a complete sample of 228 radio-quiet non-BAL quasars more than 80% of which were detected in medium-deep pointed observations with ROSAT. The slope of $0.65 \pm 0.02$ which they quote for the $\log L_{2\mathrm{keV}} - \log L_{2500}$ relation is in excellent agreement with the values we find for all our samples when we fit our "total" stacks without allowing for evolution [equation (10)]. However, after allowing for evolution, our analysis predicts a shallower value, $0.53 \pm 0.02$, both from our individual detections and from our "total" stacks. This is a consequence of the significant evolution we detect, together with the strong selection-induced correlation between optical luminosity and redshift in our samples. Moreover, since $\log L_{2\mathrm{keV}}$ is normally distributed with a scatter of about 0.40, the median $L_{2\mathrm{keV}}$ at given $L_{2500}$ is smaller than the mean by a factor of about 1.7. The excellent apparent agreement in Fig. 7 between the Strateva et al. relation and our own RQQ relation is thus misleading. The Strateva et al. result gives median $L_{2\mathrm{keV}}$ as a function of $L_{2500}$ since they fit in logarithm space; on the other hand, our result gives the mean $L_{2\mathrm{keV}}$ of QSOs of given $L_{2500}$. Thus the relations should be off-set by a factor of 1.7. Quasar variability could perhaps account for this discrepancy given the longer X-ray exposure times in the Strateva et al. (2005) data. QSOs vary on time-scales of $\sim 10^4$ seconds at X-ray wavelengths with typical amplitudes of about 0.2 in $\log L_{2\mathrm{keV}}$ (e.g. Almaini et al. 2000; Manners, Almaini & Lawrence 2002). In our study such variability contributes to the scatter in the $L_{2\mathrm{keV}}$ distribution at given optical luminosity, since exposure times for our quasars are shorter than $\sim 10^4$s. Studies

based on longer X-ray exposures should find a distribution with a higher median and lower scatter (but with the same mean). It is suggestive that Strateva et al. find a smaller scatter in $\log L_{2\mathrm{keV}}$ than we do, 0.29 (see Fig. 14 in their paper) rather than 0.40.

La Franca et al. (1995) and Yuan, Siber & Brinkmann (1997) argued that photometric error in the optical luminosities might cause an apparently weaker than linear dependence of $L_X$ on $L_O$, even if the true relation is linear. This explanation is no longer tenable for data of the quality analysed here [or indeed in Strateva et al. (2005)]. The relations we find really are much weaker than linear, $\tilde{L}_{2\mathrm{keV}} \propto L_{2500}^{0.53}$(RQQs) and $\tilde{L}_{2\mathrm{keV}} \propto L_{[\mathrm{OIII}]}^{0.33}$. The difference between the slopes for the two different optical measures of quasar activity is large and interesting.

The most important assumption in our study which still remains to be fully justified observationally is the log-normal form we adopt for the distribution of $L_{2\mathrm{keV}}$ at given optical luminosity. As shown by Figures 10 and 12, all the observational data (e.g. the fraction of individually detected objects, the distribution of their $L_{2\mathrm{keV}}$, the mean $L_{2\mathrm{keV}}$ both for stacks of all sources and for stacks of individually undetected sources) appear consistent with this assumption, but they do not constrain the shape of the distribution at low X-ray luminosities. Note, however, that the part of the distribution we can characterize well already corresponds to more than 50% of the sources and to about 75% of their total X-ray output. Our log-normal hypothesis will be more thoroughly tested by future X-ray studies which will simultaneously achieve wide area coverage and deep sensitivity limits, resulting in much greater detection completeness than is possible with the RASS.

(MPA), the Max-Planck-Institute for Astrophysics (MPIA), New Mexico State University, Ohio State University, University of Pittsburgh, University of Portsmouth, Princeton University, the United States Naval Observatory, and the University of Washington.

## REFERENCES

Almaini O., Lawrence T.S., Edge A., Boyle B.J., Georgantopoulos I., Gunn K.F., Stewart G.C., Griffiths R.E., 2000, MNRAS, 315, 325

Anderson, S.F. et al., 2003, AJ, 126, 2209

Anderson S.F., Margon B., 1987, 314, 111

Avni Y., Tananbaum H., 1982, ApJ, 262, 17

Avni Y., Tananbaum H., 1986, ApJ, 305, 83

Avni Y., Worrall D.M., Morgan W.A., 1995, ApJ, 454, 673

Bassett L.C., Brandt W.N., Schneider D.P., Vignali C., Chartas G., Garmire G.P., 2004, AJ, 128, 523

Bechtold J., Elvis M., Fiore F., Kuhn O., Cutri R.M., McDowell J.C., Rieke M., Siemiginowska A., Wilkes B.J., 1994, AJ, 108, 759

Bechtold J., Siemiginowska A., Shields J., Czerny B., Janiuk A., Hamann F., Aldcroft T.L.; Elvis M.; Dobrzycki A., 2003, ApJ, 588, 119

Becker R.H., White R.L., & Helfand D.J., 1995, ApJ, 450, 559

Brinkmann W., Laurent-Muehleisen S.A., Voges W., Siebert J., Becker R.H., Brotherton M.S., White R.L., Gregg M.D., 2000, A&A, 356, 445

Brinkmann W., Yuan W., Siebert J., 1997, A&A, 319 413

Dickey J.M. & Lockman F.J., 1990, ARA&A, 28,215

Franceschini A., La Franca F., Cristiani S., Martin-Mirones J.M., 1994, MNRAS, 269, 683

Georgakakis A., Hopkins A.M., Sullivan M., Afonso J., Georgantopoulos I., Mobasher B., Cram L.E., 2003, MNRAS, 345, 939

Green P.J., Schartel N., Anderson S.F., Hewett P.C., Foltz C.B., Brinkmann W., Fink H., Truemper J., Margon B., 1995, ApJ, 450, 51

Ivezic Z. et al., 2002, AJ, 124, 2364

Kauffmann G. et al., 2003, MNRAS, 346, 1055

Ku W.H.M., Helfand D.J., Lucy L.B., 1980, Nature, 288, 323

La Franca F., Franceschini A., Cristiani S., Vio R., 1995, 299, 19

Manners J., Almaini O., Lawrence A., 2002, MNRAS, 330, 390

Marziani P., Zamanov R.K., Sulentic J.W., Calvani M., 2003, MNRAS, 345, 1133

Nandra K., Mushotzky R.F., Arnaud K., Steidel C.C., Adelberger K.L., Gardner J.P., Teplitz H.I., Windhorst R.A., 2002, ApJ, 576, 625

Nandy K., Thompson G.I., Jamar C., Monfils A., Wilson R., 1975, A&A, 44,195

Pickering T.E., Impey C.D., Foltz C.B., 1994, AJ, 108, 1542

Pier J.R., Munn J.A., Hindsley R.B., Hennessy G.S., Kent S.M., Lupton R.H., Ivezic Z., 2003, AJ, 125, 1559

Reeves J.N., & Turner M.J.L., 2000, MNRAS 316, 234

Richards G.T. et al., 2002, AJ, 123, 2945

Richards G.T. et al., 2004, ApJS, 155, 257

Risaliti G., Elvis M., 2005, ApJ accepted, astro-ph/0507434

Schartel N., Green P.J., Anderson S.F., Hewett P.C., Foltz C.B., Margon B., Brinkmann W., Fink H., Trumper J., 1996 MNRAS, 1015,

Schlegel D.J., Finkbeiner D.P., Davis M., 1998, ApJ, 500, 525

Schneider D.P. et al., AJ, 2003, 126, 2579

Schneider D.P. et al., AJ, 2005, 130, 367

Snowden S.L., Freyberg M.J., Plucinsky P.P., Schmitt J.H.M.M.; Truemper J., Voges W., Edgar R.J., McCammon D., Sanders W.T.,1995, ApJ, 454, 643

Strateva I.V., Brandt W.N., Schneider D.P., Vanden Berk D.G., Vignali C., 2005, AJ, 130, 387

Vanden Berk D.E. et al., 2001, AJ, 122, 549

Vanden Berk D.E. et al., 2005, AJ, 129, 2047

Vignali C., Alexander D.M., Comastri A., 2004, MNRAS, 354, 720

Vignali C., Brandt W.N., Schneider D.P., 2003a, AJ, 125, 433

Vignali C., Brandt W.N., Schneider D.P., Garmire G.P., Kaspi S., 2003b, AJ, 125, 418

Voges et al., 1999, A&A 349, 389

Voges et al., 2000, IAUC, 7432

Wolf C. et al., 2004, A&A, 421, 913

Wang Q.D., 2004, ApJ, 612, 159

Worrall D.M., Tananbaum H., Giommi P., Zamorani G., 1987, ApJ, 313, 596

Wu X., & Anderson S.F., 1992, AJ, 103, 1

York D. et al., 2000, AJ, 120, 1579

Yuan W., Siebert J., Brinkmann W., 1997, A&A, 334, 498

Yuan W., Brinkmann W., Siebert J., Voges W., 1998, A&A, 330,108

Zakamska N.L., Strauss M.A., Heckman T.M., Ivezic Z., Krolik J.H., 2004, AJ, 128, 1002

Zamorani G., Henry J.P., Maccacaro T., Tananbaum H., Soltan A., Avni Y., Liebert J., and others, 1981, ApJ, 245, 357

**Table 1.** The redshift range, $i$ band magnitude limit and number of objects for each sample. $N_{tot}$ is the total number of quasars. $N_x$ is the number of these individually detected in RASS with $L > 7$. $N_S$ is the number of stacks used both when making "total" stacks of all quasars (section 4.1) and when stacking non-detections (section 4.3). $N_{S,A}$ is the number of "total" stacks detected with $L > 7$. The corresponding number for stacks of non-detections is $N_{S,U}$. The samples labelled with [OIII] are for quasars with [OIII]$\lambda$5007 measured.

| Sample | redshift | magnitude | $N_{tot}$ | $N_x$ | $N_S$ | $N_{S,A}$ | $N_{S,U}$ |
|---|---|---|---|---|---|---|---|
| All | $0.08 < z < 5.41$ | $i < 20.5$ | 46420 | 3120 | 209 | 199 | 194 |
| RLQs | $0.10 < z < 5.31$ | $i < 20.5$ | 3206 | 341 | 51 | 50 | 49 |
| RQQs | $0.08 < z < 4.98$ | $i < 19.1$ | 25705 | 2034 | 118 | 117 | 117 |
| [OIII] | $z < 0.80$ | $i < 20.5$ | 9103 | 2192 | 141 | 141 | 141 |
| [OIII] RLQs | $z < 0.80$ | $i < 20.5$ | 587 | 181 | 26 | 25 | 25 |
| [OIII] RQQs | $z < 0.80$ | $i < 19.1$ | 5880 | 1509 | 90 | 90 | 90 |

**Table 2.** Estimates and 1-$\sigma$ confidence ranges for the model parameters in equations (9), (13), (14), (23) and (24) from $\chi^2$ fitting of the "total" stacks.

| Case | equation | $\alpha$ | $\beta$ | $\gamma$ | $z_0$ | $\delta$ | $\chi^2_{min}$ |
|---|---|---|---|---|---|---|---|
| ALL | (9) | $0.64^{+0.01}_{-0.01}$ | — | — | — | $26.63^{+0.01}_{-0.01}$ | 306.0 |
| ALL | (13) | $0.52^{+0.02}_{-0.02}$ | $0.67^{+0.09}_{-0.09}$ | — | — | $26.51^{+0.02}_{-0.01}$ | 269.1 |
| ALL | (14) | $0.51^{+0.02}_{-0.02}$ | $1.89^{+0.33}_{-0.33}$ | $0.54^{+0.08}_{-0.12}$ | $0.56^{+0.08}_{-0.04}$ | $26.55^{+0.02}_{-0.01}$ | 250.0 |
| RQQ | (9) | $0.68^{+0.01}_{-0.01}$ | — | — | — | $26.53^{+0.01}_{-0.01}$ | 213.3 |
| RQQ | (13) | $0.57^{+0.02}_{-0.03}$ | $0.57^{+0.16}_{-0.12}$ | — | — | $26.44^{+0.02}_{-0.02}$ | 200.5 |
| RQQ | (14) | $0.54^{+0.02}_{-0.04}$ | $2.04^{+0.72}_{-0.52}$ | $0.54^{+0.18}_{-0.14}$ | $0.48^{+0.08}_{-0.06}$ | $26.44^{+0.03}_{-0.03}$ | 190.7 |
| RLQ | (9) | $0.65^{+0.02}_{-0.03}$ | — | — | — | $26.91^{+0.02}_{-0.01}$ | 35.2 |
| RLQ | (13) | $0.63^{+0.05}_{-0.06}$ | $0.12^{+0.28}_{-0.29}$ | — | — | $26.89^{+0.05}_{-0.05}$ | 35.0 |
| [OIII] ALL | (24) | $0.46^{+0.02}_{-0.02}$ | — | — | — | $26.18^{+0.01}_{-0.01}$ | 209.2 |
| [OIII] ALL | (23) | $0.33^{+0.02}_{-0.02}$ | $2.68^{+0.18}_{-0.24}$ | — | — | $25.68^{+0.04}_{-0.03}$ | 97.2 |
| [OIII] RLQ | (24) | $0.55^{+0.07}_{-0.07}$ | — | — | — | $26.36^{+0.04}_{-0.04}$ | 13.5 |
| [OIII] RLQ | (23) | $0.45^{+0.08}_{-0.08}$ | $2.38^{+0.96}_{-1.03}$ | — | — | $25.91^{+0.19}_{-0.17}$ | 8.7 |
| [OIII] RQQ | (24) | $0.49^{+0.03}_{-0.02}$ | — | — | — | $26.10^{+0.01}_{-0.01}$ | 141.6 |
| [OIII] RQQ | (23) | $0.32^{+0.02}_{-0.03}$ | $3.26^{+0.29}_{-0.26}$ | — | — | $25.49^{+0.05}_{-0.05}$ | 39.1 |

**Table 3.** Maximum likelihood estimates and 1-$\sigma$ confidence ranges for the model parameters in equations (14) and (23).

| Case | equation | $\alpha$ | $\beta$ | $\gamma$ | $z_0$ | $\delta$ |
|---|---|---|---|---|---|---|
| RLQ | (14) | $0.58^{+0.03}_{-0.03}$ | $3.39^{+1.75}_{-1.45}$ | $0.47^{+0.16}_{-0.20}$ | $0.39^{+0.06}_{-0.06}$ | $26.66^{+0.14}_{-0.08}$ |
| RQQ | (14) | $0.66^{+0.01}_{-0.02}$ | $0.71^{+0.24}_{-0.26}$ | $-0.48^{+0.12}_{-0.11}$ | $0.55^{+0.04}_{-0.02}$ | $26.28^{+0.02}_{-0.02}$ |
| ALL | (14) | $0.53^{+0.02}_{-0.01}$ | $1.81^{+0.28}_{-0.14}$ | $0.40^{+0.10}_{-0.06}$ | $0.59^{+0.04}_{-0.01}$ | $26.30^{+0.01}_{-0.02}$ |
| [OIII] RLQ | (23) | $0.29^{+0.04}_{-0.05}$ | $3.12^{+0.54}_{-0.54}$ | — | — | $25.44^{+0.02}_{-0.02}$ |
| [OIII] RQQ | (23) | $0.34^{+0.01}_{-0.01}$ | $3.14^{+0.18}_{-0.16}$ | — | — | $25.25^{+0.01}_{-0.01}$ |
| [OIII] ALL | (23) | $0.31^{+0.01}_{-0.01}$ | $3.22^{+0.12}_{-0.14}$ | — | — | $25.31^{+0.01}_{-0.01}$ |